The Astrophysical Journal, 680:246–262, 2008 June 10

SUBMILLIMETER GALAXIES AT $z \sim 2$: EVIDENCE FOR MAJOR MERGERS AND CONSTRAINTS ON LIFETIMES, IMF, AND CO-H_2 CONVERSION FACTOR[1]

L. J. Tacconi,[2] R. Genzel,[2,3] I. Smail,[4] R. Neri,[5] S. C. Chapman,[6] R. J. Ivison,[7] A. Blain,[8] P. Cox,[5] A. Omont,[9] F. Bertoldi,[10] T. Greve,[11] N. M. Förster Schreiber,[2] S. Genel,[2] D. Lutz,[2] A. M. Swinbank,[4] A. E. Shapley,[12] D. K. Erb,[13] A. Cimatti,[14] E. Daddi,[15] and A. J. Baker[16]

Received 2007 November 13; accepted 2008 January 23

ABSTRACT

We report subarcsecond resolution IRAM PdBI millimeter CO interferometry of four $z \sim 2$ submillimeter galaxies (SMGs), and sensitive CO(3–2) flux limits toward three $z \sim 2$ UV/optically selected star-forming galaxies. The new data reveal for the first time spatially resolved CO gas kinematics in the observed SMGs. Two of the SMGs show double or multiple morphologies, with complex, disturbed gas motions. The other two SMGs exhibit CO velocity gradients of $\sim$500 km s^{-1} across $\leq 0.2''$ (1.6 kpc) diameter regions, suggesting that the star-forming gas is in compact, rotating disks. Our data provide compelling evidence that these SMGs represent extreme, short-lived "maximum" star-forming events in highly dissipative mergers of gas-rich galaxies. The resulting high-mass surface and volume densities of SMGs are similar to those of compact quiescent galaxies in the same redshift range and much higher than those in local spheroids. From the ratio of the comoving volume densities of SMGs and quiescent galaxies in the same mass and redshift ranges, and from the comparison of gas exhaustion timescales and stellar ages, we estimate that the SMG phase duration is about 100 Myr. Our analysis of SMGs and optically/UV selected high-redshift star-forming galaxies supports a "universal" Chabrier IMF as being valid over the star-forming history of these galaxies. We find that the ^{12}CO luminosity to total gas mass conversion factors at $z \sim 2$–3 are probably similar to those assumed at $z \sim 0$. The implied gas fractions in our sample galaxies range from 20% to 50%.

Subject headings: cosmology: observations — galaxies: evolution — galaxies: formation — galaxies: high-redshift — galaxies: kinematics and dynamics — stars: luminosity function, mass function

Online material: color figures

1. INTRODUCTION

Deep surveys have become efficient in detecting and studying $z \sim 1.5$–3 star-forming galaxy populations (e.g., Steidel et al. 1996, 2004; Franx et al. 2003; Daddi et al. 2004a; Hughes et al. 1998; Chapman et al. 2005). Fairly large samples are now available based on their rest-frame UV magnitude/color properties, for example, the $z \sim 3$ Lyman break galaxies (LBGs; e.g., Steidel et al. 1996) and the $z \sim 1.4$–2.5 BX/BM galaxies (e.g., Adelberger et al. 2004; Steidel et al. 2004; Erb et al. 2006b). Other samples have been chosen based on their rest-frame optical magnitude/color properties, such as the $z \sim 1.4$–2.6 "star-forming" or "sBzKs" (e.g., Daddi et al. 2004a, 2004b; Kong et al. 2006) or distant red galaxies (DRGs; Franx et al. 2003). Finally, dusty luminous high-redshift galaxies at $z \sim 1$–3.5 have been unveiled through their high submillimeter flux densities (e.g., Smail et al. 2002; Chapman et al. 2003, 2005; Pope et al. 2005). These bright, submillimeter continuum-selected systems (SMGs) with $S_{850\,\mu m} > 5$ mJy are dusty and gas-rich, very luminous ($\sim 10^{13}\,L_\odot$) galaxies with star formation rates SFR $\sim 10^3\,M_\odot$ yr^{-1} (Blain et al. 2002; Smail et al. 2002; Chapman et al. 2005). In contrast, the BX/BM or sBzK/DRG selection criteria sample luminous ($L \sim 10^{11}$–$10^{12}\,L_\odot$) galaxies with SFR $\sim$ 10–500 $M_\odot$ yr^{-1}, and with estimated ages from 50 Myr to 2 Gyr (e.g., Erb et al. 2006a, 2006b, 2006c; Förster Schreiber et al. 2004; Daddi et al. 2004a, 2004b; Papovich et al. 2007).

For the SMGs, Chapman et al. (2003, 2005) and Swinbank et al. (2004) have been able to obtain rest-frame UV/optical

[1] Based on observations obtained at the IRAM Plateau de Bure Interferometer (PdBI). IRAM is funded by the Centre National de la Recherché Scientifique (France), the Max-Planck Gesellschaft (Germany), and the Instituto Geografico Nacional (Spain).

[2] Max-Planck Institut für Extraterrestrische Physik (MPE), Giessenbachstrasse 1, D-85741 Garching, Germany; linda@mpe.mpg.de, genzel@mpe.mpg.de, forster@mpe.mpg.de, shy@mpe.mpg.de, lutz@mpe.mpg.de.

[3] Department of Physics, University of California, Le Conte Hall, Berkeley, CA, 94720.

[4] Institute for Computational Cosmology, Durham University, Durham, United Kingdom; ian.smail@durham.ac.uk, a.m.swinbank@dur.ac.uk.

[5] Institut de Radio Astronomie Millimetrique (IRAM), St. Martin d'Heres, France; neri@iram.fr, pierre.cox@iram.fr.

[6] Institute of Astronomy, University of Cambridge, Madingley Road, Cambridge, CB3 0HA, United Kingdom; schapman@ast.cam.ac.uk.

[7] UK Astronomy Technology Centre, Royal Observatory, Blackford Hill, Edinburgh EH9 3HJ, United Kingdom and Institute for Astronomy, University of Edinburgh, Blackford Hill, Edinburgh EH9 3HJ, United Kingdom; rji@roe.ac.uk.

[8] Astronomy 105-24, California Institute of Technology, Pasadena, CA 91125; awb@astro.caltech.edu, schapman@irastro.caltech.edu.

[9] CNRS and Institut d'Astrophysique de Paris, 98 bis boulevard Arago, 75014 Paris, France; omont@iap.fr.

[10] AIUB, Bonn, Germany; bertoldi@astro.uni-bonn.de.

[11] Max-Planck Institut für Astronomie (MPIA), Königsstuhl 17, D-68117 Heidelberg, Germany; tgreve@mpia.de.

[12] Department of Astrophysical Sciences, Princeton University, Peyton Hall, Princeton, NJ 08544; aes@astro.princeton.edu.

[13] Harvard-Smithsonian Center for Astrophysics, 60 Garden Street, Cambridge, MA 02138; derb@cfa.harvard.edu.

[14] Dipartimento di Astronomia–Alma Mater Studiorum–Università di Bologna, Via Ranzani 1, I-40127 Bologna, Italy; a.cimatti@unibo.it.

[15] Laboratoire AIM, CEA/DSM-CNRS–Université Paris Diderot, DAPNIA/SAp, Orme des Merisiers, 91191 Gif-sur-Yvette, France; emanuele.daddi@cea.fr.

[16] Department of Physics and Astronomy, Rutgers, State University of New Jersey, 136 Frelinghuysen Road Piscataway, NJ 08854; ajbaker@physics.rutgers.edu.

redshifts for 73 SMGs detected with the SCUBA and MAMBO cameras at 850 μm and 1.2 mm. In comparison to earlier attempts, this effort has succeeded thanks to precise positions derived from deep 1.4 GHz VLA observations of the same fields (Ivison et al. 2002; Chapman et al. 2003). Starting from these results, some of us have been carrying out a survey at the IRAM Plateau de Bure millimeter interferometer (PdBI), where we successfully detected molecular emission and determined line profiles in the CO(3–2) and (4–3) rotational lines for 18 of these SMGs (Neri et al. 2003; Greve et al. 2005; Tacconi et al. 2006; I. Smail et al., in preparation). Tacconi et al. (2006) presented subarcsecond resolution PdBI millimeter imaging of six of the program SMGs and showed that several of these sources were surprisingly compact ($R_{1/2} \leq 2$ kpc) and that SMGs are "maximum starbursts," that is, systems in which a significant fraction of the available initial gas reservoir of 10^{10}–10^{11} $M_\odot$ is converted to stars over several dynamical timescales, typically of the order of a few times 10^8 yr. The SMGs appear to be scaled-up versions of the local ultraluminous infrared galaxy population (Sanders & Mirabel 1996).

Significant progress has been made in elucidating the physical properties of high-z star-forming galaxies, as well as the relations of different populations to each other (e.g., Reddy et al. 2005; Grazian et al. 2007; Bouché et al. 2007). However, one important open issue is the stellar initial mass function (IMF) at high redshift (e.g., Renzini 2005; van Dokkum 2007; Davé 2008). An empirical determination of the IMF (slope, lower and upper mass range, mass to light ratio) in high-z star-forming galaxies would obviously be of substantial interest for future galaxy evolution studies. Various arguments based on the M_*/L_B ratio of $z \sim 0$ ellipticals, the slope and zero point of the $z = 0$–1.3 fundamental plane of spheroids in galaxy clusters, and the metal abundances in galaxy clusters suggest that the Milky Way IMF (Kroupa 2001; Chabrier 2003) may be universally applicable, at least to moderate redshifts (Renzini 2005). On the other hand, there is good evidence that in the massive, dense Arches and NGC 3603 star clusters and the Galactic center nuclear cluster the IMF is top-heavy. For NGC 3603, Stolte et al. (2002) and Harayama et al. (2008) find a power-law slope of the IMF of $\gamma = 1.7$,[17] where Salpeter, Kroupa, and Chabrier IMFs have $\gamma = 2.3$–2.35 for $m \geq 1$ $M_\odot$. In the central parsec of the Milky Way, Nayakshin & Sunyaev (2005) and Paumard et al. (2006) infer $\gamma \sim 1$. Baugh et al. (2005) conclude that a top-heavy IMF ($\gamma \sim 1$) is required to fit the number counts of SMGs in their semianalytic models (Lacey et al. 2008). Without a normal Galactic IMF, the Baugh et al. (2005) models miss the observed number counts by factors of between 20 and 40. Extending these models to include metallicities and supernova feedback, Nagashima et al. (2005) conclude that a top-heavy IMF also better fits the observed supersolar [O/Fe] abundance ratios of massive ellipticals. More recently, Lacey et al. (2008) confirm and extend this conclusion when fitting in addition the luminosity function of *Spitzer* 24–160 μm counts. Finally, van Dokkum (2007) and Davé (2008) discuss further possible evidence and motivation for the IMF to be more top-heavy at high redshift than it is locally. To test these proposals, it is obviously of interest to obtain a direct constraint on the high-z IMF.

In the present paper we follow up on the work of Tacconi et al. (2006) and increase the angular resolution of the PdBI observations by another factor of 2, to 0.25″–0.5″ FWHM. For four of the $z \sim 2$ SMGs we now resolve the compact sources *and* their CO kinematics. We find compelling kinematic evidence for highly dissipative mergers and orbital motion on scales of <1 kpc and set new constraints on the physical properties and evolution of these SMGs. We also report sensitive limits on CO emission toward three representatives of the UV/optically star-forming population at $z \sim 2$. For the standard $H = 70$ km s^{-1} Mpc^{-1}, $\Omega_m = 0.3$ ΛCDM cosmology adopted here, 1″ corresponds to 8.2 kpc at $z = 2.2$.

[17] Here we define the IMF in terms of the number of stars in the mass interval between m_*, and $m_* + dm_*$. For a single power law IMF this number would be $dN(m_*) \sim m_*^{-\gamma}\, dm_*$.

2. OBSERVATIONS

The submillimeter galaxy observations were carried out in two seasons (winter 2005/2006 and 2006/2007) with the PdBI (Guilloteau et al. 1992), which consists of six 15 m diameter telescopes. For our high-resolution observations in the new extended A configuration (760 m baseline) we selected four galaxies of the $S_{850\,\mu m} \geq 5$ mJy radio-detected SCUBA sample (Chapman et al. 2005). We had previously observed all four galaxies with the PdBI in the shorter baseline configurations (Neri et al. 2003; Greve et al. 2005; Tacconi et al. 2006). Weather conditions during the observations were excellent. We observed the galaxies HDF 242 (SMM J123707+6214, $z = 2.49$; Chapman et al. 2003; 2005; Swinbank et al. 2004; Tacconi et al. 2006) and N2850.4 (SMM J16350+4057, $z = 2.39$; Ivison et al. 2002; Smail et al. 2003; Neri et al. 2003; Chapman et al. 2005) in 2006 January–February. For this period, the array was equipped with both (single-sideband) 3 mm and (double-sideband) 1 mm SIS receivers that we used simultaneously. System temperatures (referred to above the atmosphere) were 110–160 K and 350–500 K at 3 and 1 mm, respectively. We observed HDF 76 (SMM J123549+6215, $z = 2.20$; Chapman et al. 2005; Swinbank et al. 2004; Tacconi et al. 2006) and N2850.2 (SMM J163658+4105, $z = 2.45$; Ivison et al. 2002; Greve et al. 2005; Chapman et al. 2005; Tacconi et al. 2006) in 2007 February with IRAM's new dual-polarization receivers at 1 mm. Typical system temperatures were 200–250 K. After combination of the two polarization channels, the new receivers yield an improvement of nearly a factor of 3 in signal-to-noise ratio for line observations at 1 mm compared to the old receivers for the same integration time and spectral resolution.

Where possible, we combined the new extended A configuration data with our previous A and B configuration observations (Tacconi et al. 2006; Greve et al. 2005; Neri et al. 2003) to maximize the sensitivity and UV coverage of the maps and to ensure that no flux was resolved out at the highest resolution. In the following, the total integration times include the lower resolution configuration observations. For data taken prior to 2007 January, the correlator was configured for line and continuum observations to cover simultaneously 580 MHz in each of the 3 mm and 1.3 mm bands. For observations taken with the new generation receivers (after 2007 January) the full available correlator capacity was configured to cover 1 GHz in each polarization. For N2850.4 the total on source integration was 40 hr ($\sim$15 hr in the extended A configuration). For N2850.2 we only included data from the new receivers, since we did not have usable 1 mm data from previous runs, and the new data from the new generation receivers were of such excellent quality. In this case the on-source integration time was 9 hr in the extended A configuration. For the sources in the Hubble Deep Field–North, HDF 76 and HDF 242 we combined data from present and past observing runs. The total integration times were 23 hr (12 hr in extended A) and 38 hr (15 hr in extended A), for HDF 76 and HDF 242, respectively.

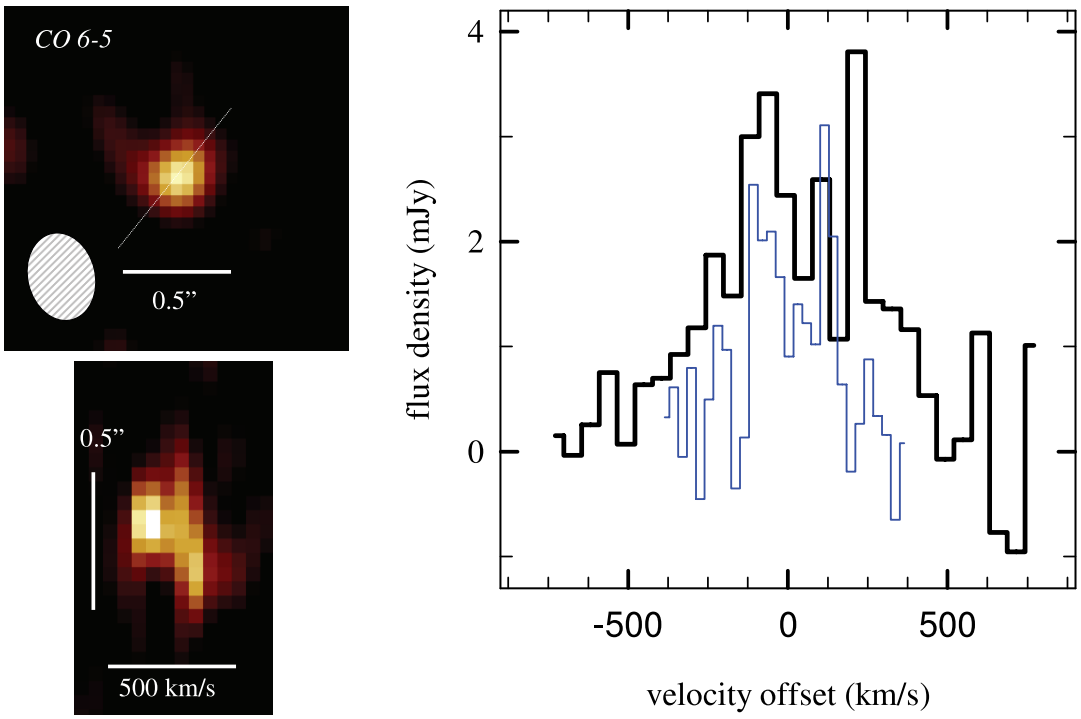

FIG. 1.— Integrated CO(6–5) line map (*top left*) and position velocity diagram (*bottom left*) along position angle −42° (*dotted line in top left*) in the source HDF 76 at $z = 2.2$. The angular resolution is $0.42'' \times 0.29''$ at a P.A. $= -168°$ FWHM (*hatched ellipse*). The position velocity diagram was smoothed with a 100 mas/110 km s^{-1} Gaussian kernel. *Right*: The integrated CO(3–2) spectrum (*black*, from Tacconi et al. 2006) and CO(6–5) spectrum (*blue*, scaled by 0.25 to be on the same Rayleigh-Jeans brightness temperature scale).

During the 2005/2006 and 2006/2007 seasons we also observed three UV/optically selected star-forming galaxies in the same redshift range as the SMGs. Two of these are so-called BX galaxies, which are selected on the basis of their rest-frame UV colors and magnitudes (“UV bright”), Q1623 BX 453 ($z = 2.18$) and Q2343 BX 389 ($z = 2.17$). These sources were taken from the near-IR long slit spectroscopic sample of Erb et al. (2006b, 2006c; see also Förster Schreiber et al. 2006; Law et al. 2007). The third source, BzK 15504, is a so called sBzK star-forming galaxy, which is selected based on its K-band magnitude ($K \leq 20$: K bright) and its UV/optical colors (Kong et al. 2006; Genzel et al. 2006). We observed BX 453 and BX 389 in the compact D configuration for 15 and 20 hr, respectively, and BzK 15504 for 22 hr in the B and C configurations. We observed the CO(3–2) transition, which was redshifted into the 3 mm band for all three sources. We did not detect the CO(3–2) line in any of these three galaxies, although we reached very sensitive 2 σ limits to the integrated line flux (at the line centroid and for the velocity width determined from the Hα observations) of 0.27, 0.27, and 0.17 Jy km s^{-1} for BX 453, BX 389, and BzK 15504, respectively. For comparison, the integrated CO(3–2) line fluxes of the four SMGs discussed above range between 1 and 2.3 Jy km s^{-1}.

We calibrated all data sets using the CLIC program in the IRAM GILDAS package (Guilloteau & Lucas 2000). Passband calibration used one or more bright quasars. Phase and amplitude variations within each track were calibrated out by interleaving reference observations of nearby quasars every 20 minutes. Our absolute positional accuracies are $\pm 0.2''$ or better. The overall flux scale for each epoch was set on MWC 349 (1.05 Jy at 102 GHz [2.9 mm] and 1.74 Jy at 238 GHz [1.3 mm]). After flagging bad and high phase noise data, we created data cubes with natural and uniform weighting using the GILDAS package. The resulting FWHM spatial resolutions were $\sim 1.0''$ for the 3 mm band data (2005/2006), and $0.25''$–$0.5''$ for the 1.3 mm band.

3. RESULTS

3.1. *The SMGs*

Figures 1–4 display the millimeter line maps, CO position-velocity maps and spectra in the CO(3–2) line at 3 mm, as well as the CO(6–5) or CO(7–6) lines at 1.3 mm, for the four SMGs. The CO source brightnesses are consistent with what we found in Tacconi et al. (2006) and are listed in Table 1 of that paper. As described below, two of the sources, HDF 242 and N2850.4 (Figs. 2 and 3), show at least two spatially resolved, well-separated components. The other two sources, HDF 76 and N2850.2 (Figs. 1 and 4), are compact, and both have double-peaked profiles indicative of a rotating gaseous disk. Where appropriate we also show overlays of the millimeter line emission on rest-frame UV/optical and radio images. The CO(6–5) and (7–6) lines originate from rotational levels >100 K above the ground state. They require substantial temperatures and densities to be populated. Tacconi et al. (2006) have argued on the basis of line shapes and line flux ratios that the interstellar gas in SMGs is probably sufficiently warm ($T_{\rm gas} > 35$ K) and dense [$n(\rm H_2) > 10^{3.5}$ cm^{-3}] to reach near thermal equilibrium in these levels. This conclusion is broadly consistent with the CO line flux ratios as a function of J. The effective line brightness temperature ratios CO(6–5)/CO(3–2) and CO(7–6)/CO(3–2) are close to or somewhat below unity (Figs. 1, 3, and 4), indicating that the turnover to subthermal population occurs near $J \sim 5$–6, in agreement with Weiss et al. (2005, 2007). In this case, the rotational lines up to this turnover state should provide reasonable tracers of the distribution and kinematics of the overall molecular gas in SMGs, while lines from above this state probably select somewhat denser gas (Narayanan et al. 2008). In the following we summarize the generic properties of the distributions and kinematics we derive from our new data. For a more detailed description of individual sources see Tacconi et al. (2006, and references therein).

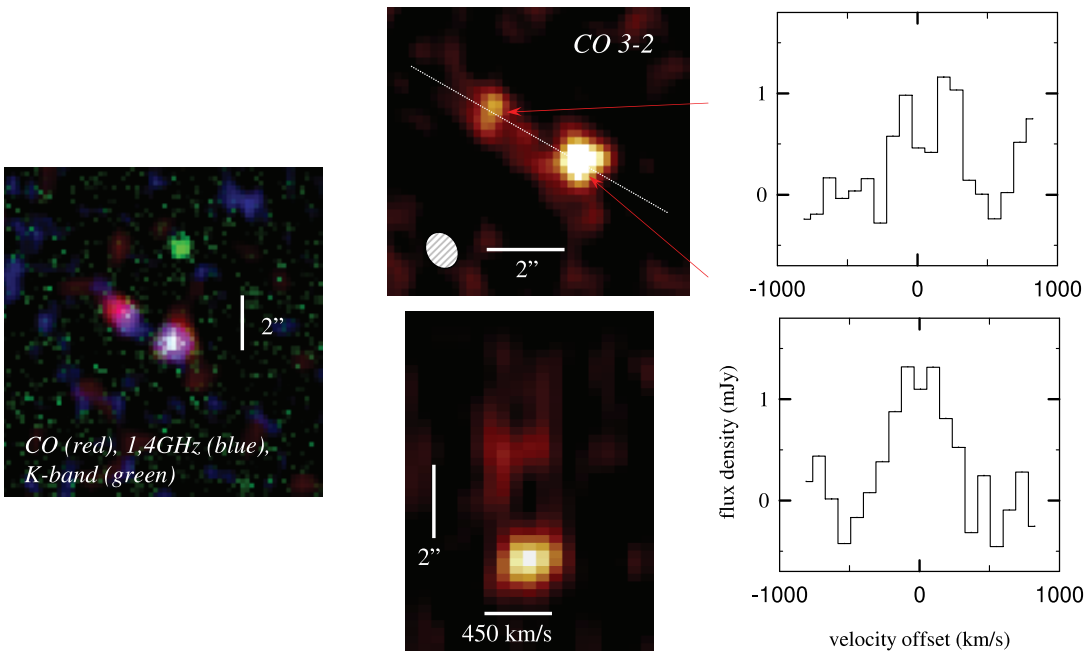

FIG. 2.— Integrated CO(3–2) line map (*top center*, angular resolution of $1'' \times 0.86''$ at P.A. $= 37^\circ$ FWHM: *hatched ellipse*) and position velocity diagram (*bottom center*) at position angle 60° (*dotted line*) of the source HDF 242 at $z = 2.49$. The position velocity diagram was smoothed with a $0.4''/185$ km s^{-1} Gaussian kernel. *Right*: CO(3–2) profiles of the two most prominent CO concentrations. *Left*: Three-color composite, with CO(3–2) in red, 1.4 GHz VLA continuum in blue (Biggs & Ivison 2008) and *K* band in green (Smail et al. 2004). The southwestern CO peak is prominent also in the rest-frame optical and radio, while the secondary northeastern CO concentration is only strongly seen in the radio continuum map. The relative astrometry of these images is accurate to $\pm 0.5''$.

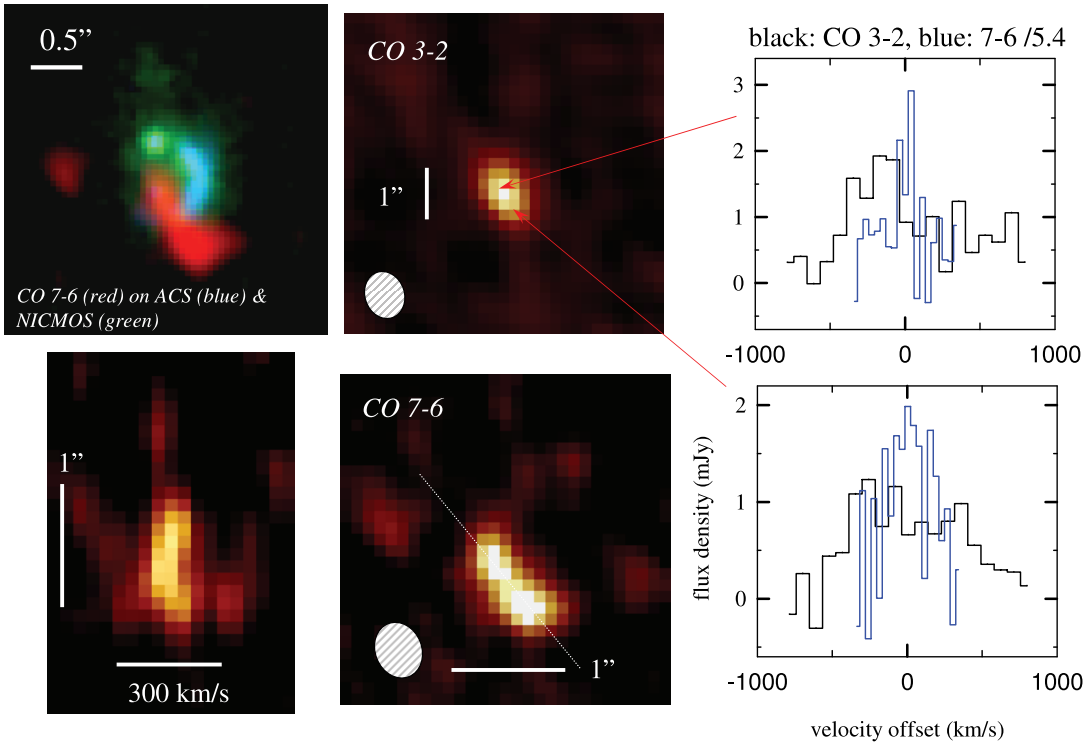

FIG. 3.— CO(3–2) (*top center*, $0.9'' \times 0.8''$ at P.A. $= 27^\circ$ FWHM: *hatched ellipse*) and CO(7–6) (*bottom center*, $0.52'' \times 0.4''$ at P.A. $= 27^\circ$ FWHM: *hatched ellipse*) integrated line maps and CO(7–6) position velocity diagram (*bottom left*) along the dotted line in the bottom central inset, in the source N2850.4 at $z = 2.39$. The position velocity diagram was smoothed with a $0.2''/74$ km s^{-1} Gaussian kernel. *Right*: CO(3–2) profiles (*black*) and CO(7–6) profiles (*blue*) toward the southwestern CO(7–6) peak (*bottom*) and northwestern CO(7–6) peak (*top*), showing a similar kinematic structure as in the CO(7–6) position velocity diagram. The CO(7–6) flux densities are scaled by 0.19 to bring CO(7–6) and (3–2) profiles on the same Rayleigh-Jeans brightness temperature scale. The top left inset shows a three-color composite of the CO(7–6) emission in red, the ACS image in blue, and the NICMOS image in green (Swinbank et al. 2005). The relative astrometry of these images is accurate to $\pm 0.5''$.

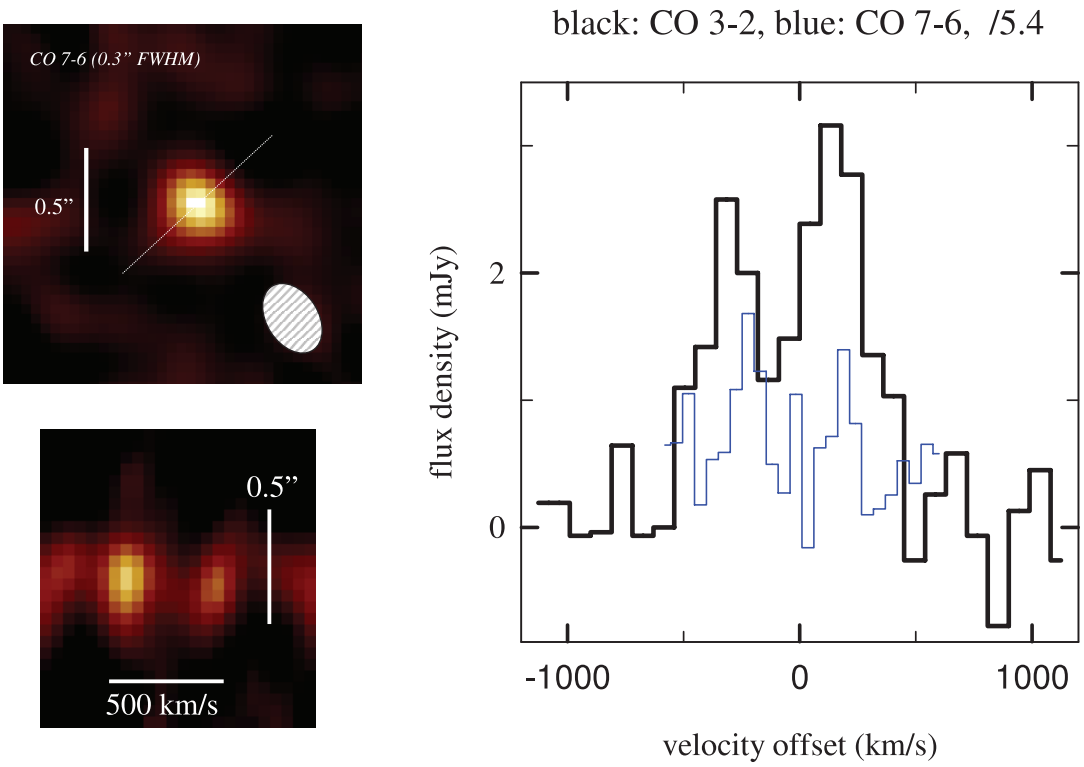

FIG. 4.—Integrated CO(7–6) line map (*top left*, $0.36'' \times 0.25''$ FWHM at P.A. $= 39°$: *hatched ellipse*) and position velocity cut (*bottom left*) in the direction marked by a dotted line in the integrated flux map, of the source N2850.2 at $z = 2.45$. The position velocity diagram was smoothed with a $0.1''/110$ km s^{-1} Gaussian kernel. *Right*: The integrated CO(3–2) (*black*: Tacconi et al. 2006) and 7–6 profiles (*blue*, scaled by 0.19 to put both lines on the same Rayleigh-Jeans brightness temperature).

3.1.1. *Spatial and Kinematic Evidence for Mergers*

We spatially resolve the CO intensity distributions and gas kinematics in all four observed SMGs. Two of our sources (HDF 242, Fig. 2; and N2850.4, Fig. 3) show well-separated, double or multiple knots on scales of $1''$–$2.5''$ (8–20 kpc). In these sources the gas kinematics are complex and unordered (bottom middle of Fig. 1 and bottom left of Fig. 2). There is no indication of simple rotation. Velocity differences between source components of 100–200 km s^{-1} are present and can be broadly understood as orbital motion, but are smaller than the line widths of the individual components, which reach $\sim$800 km s^{-1} FWHM in the southern component of N2850.4. Comparison of the CO(7–6) emission with the rest-frame UV/optical emission of N2850.4 (Fig. 2, *top left*) adds to the impression that this system is a very complex system of dense gas, massive star formation, and probably also AGN activity spread over a region of <8 kpc in diameter (see Smail et al. 2003; Swinbank et al. 2005, for details). There are strong color gradients in the source. The optical/UV emission and CO emission have very different morphologies, and their peaks are not spatially coincident (even when considering the $\pm 0.5''$ combined astrometric uncertainties). These differences are most likely the result of high, spatially variable extinction, similar to that seen in dusty $z \sim 0$ starburst galaxies (e.g., M82: Satyapal et al. 1997; Förster Schreiber et al. 2001) and ULIRGs (e.g., Scoville et al. 2000). Our findings are also in agreement with the predictions from simulations of massive mergers that aim at matching the properties of SMGs (e.g., Narayanan et al. 2006). N2850.4 is probably a late-stage, massive merger.

HDF 242 exhibits properties of an earlier stage merger; it shows two distinct galaxy systems separated by $\sim$20 kpc in projection (bottom middle of Fig. 2). The two components are both prominent in CO and radio continuum emission but only the southwestern component is clearly present on the *K*-band image (Fig. 2, *left*). There appears to be a kinematic bridge of CO emission connecting the two components (top middle and bottom middle of Fig. 2), demonstrating the physical interaction between the two systems.

Tacconi et al. (2006) discuss a third such widely separated double-nucleus system, SMM J094303+4700 ($z = 3.34$), which has two components (H6 and H7) separated by $\sim 4''$ (25 kpc). A fourth SMG with clear indications for being a dynamically interacting pair is SMM J140103+0252 (Ivison et al. 2001; Downes & Solomon 2003; Smail et al. 2005; Nesvadba et al. 2007). Together with recent Hα observations by Swinbank et al. (2006) that reveal multiple components in another four SMGs, these four systems resemble local double-nucleus ULIRGs, albeit at higher mass and luminosity (Downes & Solomon 1998; Bryant & Scoville 1999; Scoville et al. 2000; Dasyra et al. 2006).

3.1.2. *Compact Rotating Merger Remnants*

The other two SMGs (HDF 76, Fig. 1; N2850.2, Fig. 4) were the most compact SMGs in the sample studied by Tacconi et al. (2006). They exhibit prominent double-peaked CO profiles (right of Figs. 3 and 4), which are seen in about 40% of the SMGs we have studied so far (Genzel et al. 2003; Greve et al. 2005; Tacconi et al. 2006). Our new observations are beginning to spatially resolve the kinematics even in these compact sources. The CO(6–5) position velocity map of HDF 76 (Fig. 1, *bottom left*) shows a significant velocity gradient. The blue and red velocity maxima ($\Delta v = 210$ km s^{-1}) are separated in the NW-SE direction by $0.18''$ (1.4 kpc). If this velocity gradient is interpreted as rotation in a compact star-forming gas disk, the mass enclosed within 700 pc is $10^{9.6}\,M_\odot$, for an assumed inclination of 52° (§ 4.2). The resulting average mass surface and equivalent hydrogen volume densities are $10^{3.5}\,M_\odot$ pc^{-2} and 10^3 cm^{-3}. The second case is

similar but even more extreme. N2850.2 exhibits two emission peaks separated by 400 km s^{-1}. The position velocity map (Fig. 3, *bottom left*) shows a marginal spatial separation of 0.05″–0.1″ (400–800 pc) and the total line emission has an intrinsic size of about 0.2″ (1.6 kpc). The corresponding dynamical mass, surface density, and volume density are 10^{10} $M_\odot$, $10^{4.5}$ $M_\odot$ pc^{-2}, and $10^{4.2}$ cm^{-3}. These surface and volume densities are comparable to those in the dense star-forming cores of Galactic molecular clouds, or to the central nuclear gas disk(s) of the extremely compact local ULIRG Arp 220 (Downes & Solomon 1998; Sakamoto et al. 1999; Downes & Eckart 2007).

How can a mass of 10^{10} $M_\odot$, comparable to that of a $0.1M_*$ galaxy, be compressed to such a small volume? The answer to the analogous question in local ULIRGs is unequivocally that such sources are end stage, major (mass ratio $<3:1$) mergers where the compression of the gas in the final merger of the two nuclei leads to the most powerful star-forming event during the entire merger history (Barnes & Hernquist 1996; Mihos & Hernquist 1994, 1996; Downes & Solomon 1998; Bryant & Scoville 1999; Scoville et al. 2000; Genzel et al. 2001; Tacconi et al. 2002; Dasyra et al. 2006). To result in the very compact merger remnants we observe, the merger has to be highly dissipative, with a large gas fraction (see Khochfar & Silk 2006). Bouché et al. (2007) find that the $z \sim 2$–3 SMGs studied with the PdBI lie in the large v, small R sector of the velocity (v)–size (R) plane. This part of the v-r plane is otherwise completely unpopulated, requiring extremely low dark matter halo angular momentum parameters ($\lambda < 0.015$, Bouché et al. 2007). Alternatively, objects in this location may have started with a larger angular momentum but then lost it as a result of a dissipative merger.

The broad line widths of these two compact SMGs are also interesting when comparing them to CO bright quasars at similar redshift. It has been known for a few years that high-redshift SMGs typically have CO line widths that are more than a factor of 2 broader than those of QSO hosts at similar redshift and molecular gas mass (e.g., Greve et al. 2005; Carilli & Wang 2006). Carilli and Wang (2006) have suggested that this difference is more likely due to an inclination effect, where we are viewing the bright QSOs more face-on than we are the highly obscured SMGs, rather than being due to host mass and/or size differences between the QSO and SMG populations. They cite the Gaussian line profiles and the unobscured view to the AGN as evidence for this. Although the new high-resolution SMG CO data presented here cannot unequivocally solve this riddle, the small CO sizes and the double-horned line profiles of HDF 76 and N2850.2 do support an inclined disk interpretation for the broad line widths in these two sources.

In summary, all six well resolved SMGs studied with subarcsecond millimeter interferometry so far (the four reported here, as well as SMM J09431+4700 from Tacconi et al. [2006] and SMM J140103+0252 from Downes & Solomon [2003]) appear to be major mergers in various stages, similar to local ULIRGs.

3.1.3. *Relationship to Compact Quiescent Galaxies at* $z \sim 1.4$–2.6

Recent *HST* and ground-based studies show that most of the apparently massive ($K \leq 20$–21) passively evolving (= "quiescent," "passively" evolving, or "red-sequence") galaxies in the same redshift range as the SMGs are remarkably compact (Daddi et al. 2004a, 2004b, 2005; Trujillo et al. 2006, 2007; Zirm et al. 2007; Toft et al. 2007). What is the relationship between these "qBzKs" (Daddi et al. 2004b, 2005) and "qDRGs" (Zirm et al. 2007; Toft et al. 2007) and the SMG population? Figure 5 shows the comparison between these systems, and with other $z \sim 2$ star-forming galaxies (sBzK/BX/BM/sDRG), in the dynamical mass-dynamical surface density plane. To place the qBzKs/DRGs on this plot, we assumed that $M_* = M_{\rm dyn}$ (zero gas and dark matter fraction). We corrected the published total stellar masses to a Chabrier (2003) IMF (factor 0.6 from a 0.1–100 $M_\odot$ Salpeter IMF, and within 15% of a Kroupa [2001] IMF). For the sDRGs (where also no dynamical mass measurements are available), we assume that the total masses also include gas, with a gas fraction of $f_{\rm gas} \sim 0.4$, motivated by our earlier SMG results (Greve et al. 2005; Tacconi et al. 2006). For the sBzK/BX/BM galaxies from the VLT-SINFONI SINS survey we adopt the dynamical mass surface densities of Bouché et al. (2007).

It is evident that SMGs have mass surface densities comparable to those of the quiescent galaxies in the same mass and redshift range. This is especially significant for the two well-resolved, compact SMGs discussed above, N2850.2 and HDF 76, which are the two topmost black squares in Figure 5. In contrast the star-forming BzKs/BX/BM objects are much less dense and lie in the same region as low-z disks, as discussed by Bouché et al. (2007). The star-forming DRGs scatter more broadly and include systems similar in density to SMGs and qBzKs/DRGs. It is thus very plausible to conclude that the star-forming SMGs and the quiescent qBzK/DRGs in the same mass, redshift, and surface density range are related by an evolutionary sequence.

3.2. *UV/Optically Selected Galaxies*

As mentioned in § 2 we also observed three UV/optically selected $z \sim 2$ star-forming galaxies. Q2343-BX 389 ($z = 2.1737$, $K_s = 20.2$) and Q1623-BX 453 ($z = 2.1820$, $K_s = 19.8$) are from the NIRSPEC survey of Erb et al. (2006b, 2006c). Both are fairly typical representatives of the BX NIRSPEC sample in terms of Hα luminosity and estimated stellar ages (0.4–2.8 Gyr) but somewhat above the median in stellar mass (5–6×10^{10} $M_\odot$ compared to 3×10^{10} $M_\odot$) and star formation rate (60–100 $M_\odot$ yr^{-1} compared to 30 $M_\odot$ yr^{-1}). We refer to Förster Schreiber et al. (2006) for BX 389 and to Law et al. (2007) for BX 453 for discussions of the subarcsecond Hα integral field spectroscopy of these galaxies. BX 389 appears to be an almost edge-on, clumpy rotating disk with a large rotation velocity (275 km s^{-1}) and scale length ($R_{1/2} = 6$ kpc). Its dynamical mass within $R_{1/2}$ (1×10^{11} $M_\odot$) is among the largest in the BX UV-selected sample observed as part of the VLT-SINFONI SINS survey (Förster Schreiber et al. 2006; G. Cresci et al., in preparation; Bouché et al. 2007). In contrast BX 453 appears to be a dispersion dominated ($\sigma = 90$ km s^{-1}), fairly compact ($R_{1/2} = 1.7$ kpc) source of modest mass (1.7×10^{10} $M_\odot$ within $R_{1/2}$; Law et al. 2007). The optically selected source BzK 15504 ($z = 2.383$, $K_s = 19.2$) is in all respects fairly typical of the bright end ($K < 20$) of the sBzK population (Daddi et al. 2004a; Kong et al. 2006; see Supplementary Material in Genzel et al. 2006). Genzel et al. (2006) found with adaptive optics assisted integral field spectroscopy that this source has a large, globally unstable, clumpy gas disk with rotation velocity of 230 km s^{-1} and scale length 4.5 kpc. Within that radius its dynamical mass is 6.5×10^{10} $M_\odot$.

Based on their extinction-corrected Hα surface brightness the star formation surface densities in all three galaxies are $\sim$1 $M_\odot$ yr^{-1} kpc^{-2} and their total star formation rates are $\sim$60–200 $M_\odot$ yr^{-1}. Application of the Schmidt-Kennicutt relation (Kennicutt 1998) implies gas surface densities of $\sim 10^2$–10^3 $M_\odot$ pc^{-2} and gas masses of a few 10^{10} $M_\odot$. For these values, assuming the same CO luminosity–to–gas mass conversion factors as for the SMGs implies that all three galaxies should have been easily detectable with the PdBI.

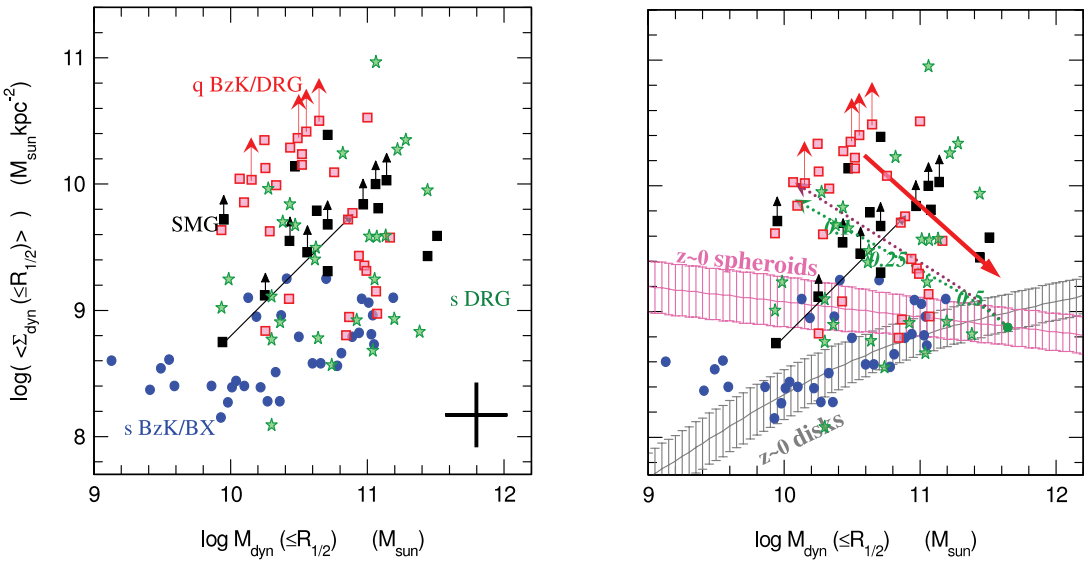

FIG. 5.—Comparison of the star-forming SMGs ($z = 1$–3.5) and various rest-frame UV/optically identified galaxy populations, in the dynamical mass-surface density plane. The horizontal axis is the dynamical mass within the half-light radius, $M_{\rm dyn}(R \le R_{1/2})$. The vertical axis is the mass surface density within the half-light radius, $\Sigma_{\rm dyn} = M_{\rm dyn}(R \le R_{1/2})/(\pi R_{1/2}^2)$. In the plots, blue circles mark the location of the star-forming BzK/BX/BM galaxies ($z = 1.4$–2.5) from the VLT-SINS survey (Bouché et al. 2007). Black squares denote the location of the SMGs from our PdBI survey (Bouché et al. 2007; this work). Arrows mark those SMGs where the present PdBI data only establish upper size limits (Tacconi et al. 2006; Smail et al. 2007), or where, in the case of SMM J140103+0252, the source is probably face-on, implying a large inclination correction to the intrinsic circular velocity (*long diagonal arrow*; Nesvadba et al. 2007). Green stars mark star-forming (s)DRGs and red squares mark quiescent qBzKs/DRGs from Daddi et al. (2005), Trujillo et al. (2006), Zirm et al. (2007), and Toft et al. (2007). The large black plus sign in the lower right denotes the typical uncertainty of these points. To bring the qBzKs/DRGs on this plot of dynamical masses and surface densities, we assumed that $M_* = M_{\rm dyn}$ for these sources but corrected the published total stellar masses to a Kroupa (2001) or Chabrier (2003) IMF by multiplying 0.1–100 $M_\odot$ Salpeter IMF based masses by 0.6. For the sDRGs we assumed that the dynamical masses also include gas, with a gas fraction of 0.4, motivated by our SMG results (Greve et al. 2005; Tacconi et al. 2006). The hatched pink and gray zones in the right inset mark the location of local spheroids and disks, respectively, from the work of Shen et al. (2003). A red arrow denotes the dry merger line, as discussed in Nipoti et al. (2003). The dotted curves show the enclosed mass (*green*) and enclosed light (*purple*) in a Hernquist (1990) profile. Numbers 0.5, 0.25, and 0.1 denote the location of the Hernquist projections within 0.5, 0.25, and 0.1 times the effective radius. The curves shown are for the specific example of a $R_{1/2} = 15$ kpc, $M_{\rm tot} = 10^{12}\ M_\odot$ system.

We did not detect the CO(3–2) line in any of these three galaxies and determined 2 σ limits to the integrated line flux (at the line centroid and for the velocity width determined from the Hα observations) of 0.27, 0.27, and 0.17 Jy km s^{-1} for BX 453, BX 389, and BzK 15504, respectively. These limits are 3–20 times lower than the integrated line fluxes of the almost two dozen SMGs observed so far (0.8–3.5 Jy km s^{-1}, I. Smail et al., in preparation). For the same CO–to–gas mass conversion factors these limits would imply remarkably low gas fractions (less than a few percent), which is difficult to understand given their large star formation rates (Erb et al. 2006b, 2006c). Alternatively, the conversion factor may be different from that in the SMGs. We explore this possibility further in § 4 and in Appendix A. Recently, Daddi et al. (2008) have successfully detected CO emission from two $z \sim 1.5$ BzK galaxies, implying molecular gas masses of several $\times 10^{10}$–$10^{11}\ M_\odot$ in these sources. These detections make our nondetections all the more puzzling, and it is not clear whether different intrinsic gas masses, star formation modes, CO-H_2 conversion factors, or some combination of these can account for the differences. Observations of a larger sample of UV/optically selected high-redshift star-forming galaxies are urgently needed to make further progress in determining the physical properties of these systems.

4. IMF AND THE CO-H_2 CONVERSION FACTOR AT $z \sim 2$

One of the issues we wish to address with our observations is to see if we can constrain the form of the IMF in high-z star-forming galaxies. In what follows we discuss a first attempt to carry out such a test on the basis of a global comparison of stellar, gas, and dynamical masses in those nine $z \sim 2$–3 SMGs, BX/sBzKs, and LBGs (see Table 1), where measurements or significant limits for all three of these input quantities are presently available.

4.1. *Dynamical Masses*

For this purpose we derived dynamical masses within the half-light radius from virial estimates (see Neri et al. 2003; Baker et al. 2004; Erb et al. 2006b, 2006c) or rotation curve models (Förster Schreiber et al. 2006; Genzel et al. 2006), including corrections for inclination. For BX 389 we applied the rotation curve modeling of Förster Schreiber et al. (2006), and for BzK 15504 the modeling of Genzel et al. (2006). For the sources lacking published velocity gradients (BX 453, cB58, and the "Cosmic Eye") we applied the usual isotropic virial estimator (e.g., Spitzer 1987)

$$M_{\rm dyn,vir}\left(R \le R_{1/2}\right) = \frac{5\sigma^2 R_{1/2}}{G}, \qquad (1)$$

where $\sigma = \Delta v_{\rm FWHM}/2.35$ is the one-dimensional velocity dispersion ($\Delta v_{\rm FWHM}$ is the FWHM integrated line width) and $R_{1/2}$ the half-light radius. For all four SMGs we applied an average of the isotropic estimator above and the "global rotating disk estimator" introduced by Neri et al. (2003), corrected for $\langle \sin(i) \rangle = \pi/4 = 1/1.273$[18] in velocity and $\langle \sin^2(i) \rangle = 2/3$ in mass, resulting in

$$M_{\rm dyn,disk}\left(R \le R_{1/2}\right) \approx 6 \times 10^4 \Delta v_{\rm FWHM}^2\left({\rm km\ s^{-1}}\right) R_{1/2}({\rm kpc}\ M_\odot). \qquad (2)$$

[18] Here we have used $\langle \sin\theta \rangle = \left(\int\int \sin\theta\, d\theta\, d\varphi\right)/\left(\int\int d\theta\, d\varphi\right) = \int_0^{\pi/2} \sin\theta\, d\theta$.

TABLE 1

PHYSICAL PROPERTIES OF $z \sim 2$–3 STAR-FORMING GALAXIES

Source (1)	Z (2)	v_c[a] (km s^{-1}) (3)	$R_{1/2}$[b] (kpc) (4)	$M_{\rm dyn}(\leq 2R_{1/2})$[c] ($10^{10}\,M_\odot$) (5)	M_*[d] ($10^{10}\,M_\odot$) (6)	$M_{\rm gas}$(CO)[e] ($10^{10}\,M_\odot$) (7)	R_*[f] ($M_\odot$ yr^{-1}) (8)	R(Hα)[g] ($M_\odot$ yr^{-1}) (9)	R(IR)[h] ($M_\odot$ yr^{-1}) (10)	t_*[i] (Myr) (11)	$t_{\rm exh}$[j] (Myr) (12)
HDF 76	2.20	384 ± 80	0.95 ± 0.4	9.4 ± 4[k]	12^{+4}_{-3}	$4 \pm 0.5\alpha$[k]	183^{+95}_{-11}	255 ± 20	900 ± 500	1000 ± 600	44α
HDF 242	2.49	275 ± 55	2.8 ± 1	24 ± 12	$12^{+2.5}_{-4.5}$	$2.9 \pm 0.5\alpha$	200^{+400}_{-65}	37 ± 11	500 ± 250	1000 ± 900	56α
N2850.2	2.45	510 ± 100	0.8 ± 0.5	14 ± 7	25 ± 7.5	$5.5 \pm 0.6\alpha$	200^{+70}_{-44}	42 ± 10	1100 ± 500	2500^{+0}_{-900}	50α
N2850.4	2.39	450 ± 90	2.4 ± 1	34 ± 14	23^{+11}_{-7}	$6.8 \pm 0.88\alpha$	460^{+260}_{-175}	190 ± 30	900 ± 450	640^{+1300}_{-320}	75α
BX Q1623−453	2.18	140 ± 73	1.7 ± 0.5	3.4 ± 1.2	4.0 ± 2	$<0.7\alpha$ ($2\,\sigma$)	130 ± 70	290 ± 170	...	400^{+400}_{-200}	$<63\alpha$
BX Q2343−389	2.17	275 ± 28	6.2 ± 2	20 ± 3	5 ± 1.5	$<0.7\alpha$ ($2\,\sigma$)	30 ± 10	210 ± 130	...	2750 ± 1000	$<140\alpha$
BzK 15504	2.38	230 ± 16	4.5 ± 1	13 ± 1.5	10 ± 2.1	$<0.5\alpha$ ($2\,\sigma$)	120^{+5}_{-40}	200 ± 100	...	1280^{+1200}_{-260}	$<34\alpha$
cB58[l]	2.73	113 ± 23	1.0 ± 0.2	1.3 ± 0.7	0.5 ± 0.1	$0.044 \pm 0.0075\alpha$	100 ± 40	...	...	50^{+20}_{-0}	4.4α
Cosmic Eye[m]	3.07	124 ± 25	1 ± 0.2	1.5 ± 0.9	1.5 ± 0.2	$0.28 \pm 0.13\alpha$	220 ± 20	...	...	100 ± 20	13α

[a] Inferred peak circular velocity, based on the work of G. Cresci et al. (in preparation), Bouché et al. (2007), Förster Schreiber et al. (2006), Genzel et al. (2006), Tacconi et al. (2006), Law et al. (2007), and this paper. Here and elsewhere, 1 σ uncertainties are shown.

[b] Intrinsic FWHM of Hα/CO emission (and uncertainty), assumed to be identical to scale length of disk. Numbers are based on the work of G. Cresci et al. (in preparation), Bouche et al. (2007), Förster Schreiber et al. (2006), Genzel et al. (2006), Tacconi et al. (2006), Law et al. (2007), and this paper.

[c] Total dynamical mass (and uncertainty), within $2R_{1/2}$.

[d] Total stellar mass (and uncertainty), from Monte Carlo fitting to the rest-frame UV/optical/near-IR spectral energy distribution, assuming a Kroupa (2001)/Chabrier (2003) IMF, stellar tracks from G. Bruzual & S. Charlot (2008, in preparation), a Calzetti et al. (2000) extinction law, and a constant or an average of constant/single stellar population star formation history. For the SMGs we adopted solar metallicity, for BzK 15504 and the BX galaxies we adopted an average of the results for 0.5 and 1.0 solar metallicity, and for the LBGs we adopted an average for the 0.2 and 0.5 solar metallicity. The photometry is from Borys et al. (2005) for HDF sources, from Ivison et al. (2002), Smail et al. (2004), and Chapman et al. (2005) for the N2850 sources, from Yee et al. (1996) and Ellingson et al. (1996) for cB58, and from Coppin et al. (2007) and Smail et al. (2007) for the "Cosmic Eye."

[e] Gas (H_2 + He) mass (and uncertainty), estimated from CO intensity and a conversion factor of $N(H_2)/I(CO) = 4.6 \times 10^{19}$ [cm^{-2}/(K km s^{-1})] [$\alpha = 1\,M_\odot$/(K km s^{-1} pc^2)], which is 0.2 times the Milky Way conversion factor. Upper limits are 2 σ.

[f] Extinction-corrected star formation rate (and uncertainty) determined from the stellar fitting above (footnote d), based on a constant star formation history and a Kroupa (2001) IMF, including correction for TP-AGB.

[g] Extinction-corrected star formation rate based on Hα (and uncertainty), using the Kennicutt (1998) conversion, but corrected for a Kroupa (2001) IMF. Note that the Calzetti et al. (2000) extinction prescription implies that the gas is extincted by a factor of 2.3 larger than the stars.

[h] Star formation rate (and uncertainty) derived from the 850 μm flux density and using the conversion SFR $= 110 S_{850\,\mu{\rm m}}$ (mJy), taken from Pope et al. (2005), for a Chabrier IMF.

[i] Stellar age, based on the stellar synthesis fitting discussed above (footnote d).

[j] Current gas exhaustion timescale, based on $M_{\rm gas}$/[SFR(FIR), SFR(Hα), SFR($*$)].

[k] The 1 σ uncertainties are given.

[l] Corrected for a lensing magnification of 31.8 (Baker et al. 2004).

[m] Corrected for a lensing magnification of 28 for the total UV/optical photometry but 8 for the CO emission (Coppin et al. 2007).

We then extrapolated to the total dynamical mass (of the star-forming regions of the galaxy) by multiplying by a factor of 2 for the above estimates, or as appropriate for the more complete (and accurate) rotation curve modeling.

4.2. *Gas Masses*

We estimated gas masses from the observed CO(3–2) line luminosities, with a suitable CO line luminosity to H_2 (+He) mass conversion factor, and assuming a brightness temperature ratio of CO(3–2) to (1–0) of unity, motivated by the findings of Weiss et al. (2005, 2007). Clearly, observations of the CO $J = 1$–0 transition with the VLA or GBT would be very useful to check this assumption (e.g., Hainline et al. 2006; Riechers et al. 2006). As discussed in more detail in Appendix A and Downes et al. (1993), the relationship between integrated CO line flux $F_{\rm CO}$ (Jy km s^{-1}) and total H_2 (+He) cold gas mass can be expressed as

$$\frac{M_{\rm gas}}{M_\odot} = 1.75 \times 10^9 \left(\frac{\alpha}{\alpha_{\rm G}}\right) \left(\frac{F_{\rm CO}}{\rm Jy\ km\ s^{-1}}\right) \times \left(\frac{T_{\rm CO(3-2)}/T_{\rm CO(1-0)}}{1}\right) (1+z)^{-3} \left(\frac{\lambda_{\rm obs}}{\rm mm}\right)^2 \left(\frac{D_L}{\rm Gpc}\right)^2, \quad (3)$$

where $T_{\rm CO(3-2)}$ and $T_{\rm CO(1-0)}$ are the effective brightness temperatures of the CO(3–2) and (1–0) lines, respectively, $\lambda_{\rm obs}$ is the wavelength of the observed (3–2) line, D_L is the luminosity distance of the galaxy and $\alpha/\alpha_{\rm G}$ is a conversion factor in units of that of the Milky Way disk. Appendix A discusses the current state of knowledge of this conversion factor in different Galactic and extragalactic environments in the local universe. There is fairly strong evidence from various measurements as well as theoretical considerations that the conversion factor in starburst galaxies, galactic nuclei and ultraluminous mergers with large gas surface densities is significantly smaller than the one in the Milky Way disk (Downes & Solomon 1998; Scoville et al. 1997). On the other hand, there is also evidence that the conversion factor may increase with decreasing metallicity, at least for the more diffuse molecular gas of nearby galaxies (e.g., Israel 2000, 2005). In our parameter search discussed below we adopted several plausible combinations of conversion factors that are suggested from these empirical $z = 0$ data.

4.3. *Stellar Masses*

We have modeled the observed spectral energy distribution of the four SMGs discussed above, as well as the $z \sim 3$ Lyman break galaxies cB58 (Baker et al. 2004) and the "Cosmic Eye" (Coppin et al. 2007; Smail et al. 2007) and the $z \sim 2$ star-forming galaxies BX 453, BX 389, and BzK 15504, with the stellar population synthesis technique described in Förster Schreiber et al. (2004). The data used includes optical and near-infrared photometry from the literature for all sources (see captions to Figs. 6–8), and mid-infrared fluxes for a subset. Briefly, the modeling procedure determines the stellar evolutionary model

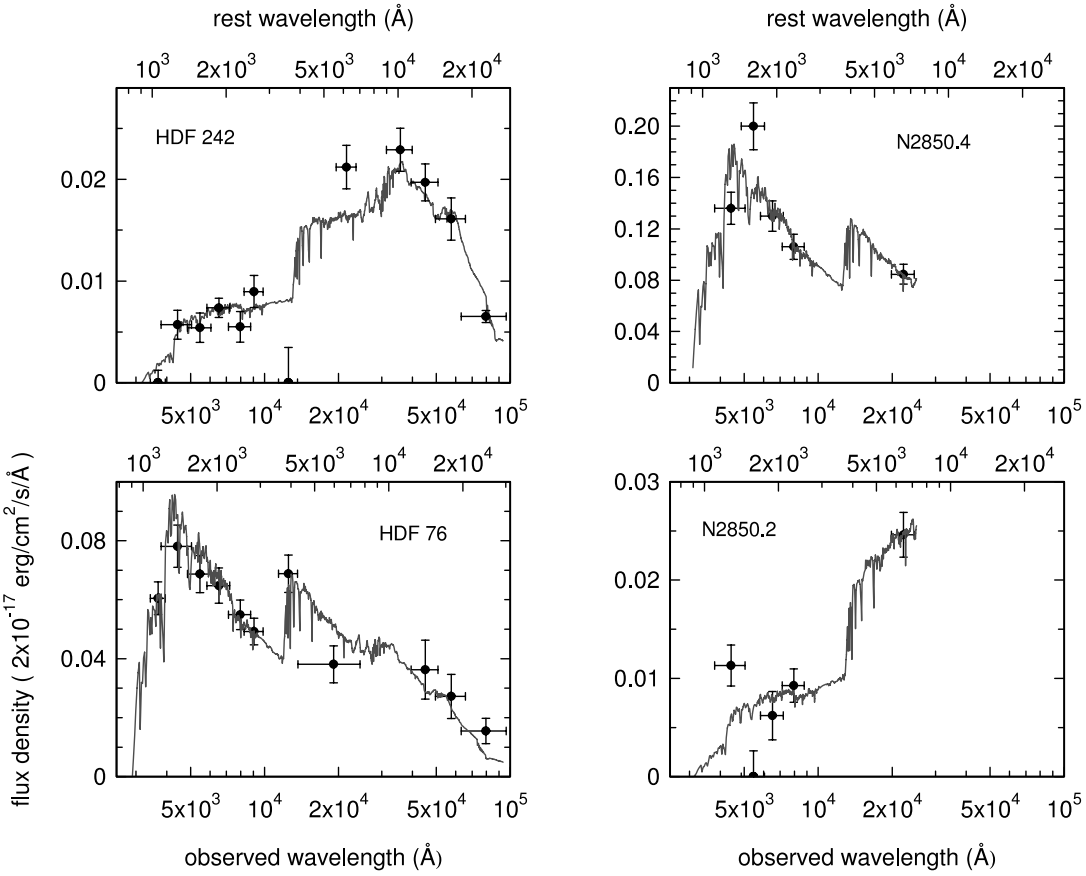

FIG. 6.—Rest-frame UV to near-infrared spectral energy distributions of the four SMGs discussed in this paper, along with best-fitting constant star formation models and stellar ages, as discussed in the text. The photometric data points are from Borys et al. (2005) for the two HDF sources, and from Smail et al. (2004), Ivison et al. (2002), and Chapman et al. (2005) for the two ELAIS N2 sources. Stellar masses quoted are for a Chabrier (2003) IMF and solar metallicity tracks; they include a correction for foreground extinction by the Milky Way. For the best-fitting star formation history parameters and masses see Table 1. [*See the electronic edition of the Journal for a color version of this figure.*]

with a synthetic spectrum that best reproduces the observed photometry. We used the recent models by S. Charlot & G. Bruzual (2008, in preparation), which feature, among other things, an improved treatment of the thermally pulsing asymptotic giant branch (AGB) phase compared to the previous Bruzual & Charlot (2003) models (see Bruzual 2007). The new models are now in good agreement with those of Maraston et al. (2006). However, in reality we do not find great differences between the stellar masses obtained with the new S. Charlot & G. Bruzual models (2008, in preparation) and those obtained with the 2003 models. We adopted the reddening prescription of Calzetti et al. (2000) and ran models for 0.2, 0.5, and 1 times solar metallicity. The free parameters were the stellar age, the interstellar extinction, and the flux scaling factor that determines the stellar mass, star formation rate, and luminosities. The flux scaling factor was fit using all photometric points. We ran models for a range of star formation histories, including an instantaneous burst ("single stellar population"), models with exponentially declining star formation rates with $1/e$ timescales ranging from of 10 Myr to 1 Gyr, and models with constant star formation rates. We used a Chabrier (2003) stellar initial mass function, which is equivalent to a Kroupa (2001) IMF to within about 15%. The best-fit properties and 68% confidence intervals for each source and set of fixed parameters were derived from 200 Monte Carlo simulations, perturbing the input photometry within the 1 σ measurement uncertainties, assuming they are Gaussian.

Figures 6–8 show the best-fitting models, all of which assume a constant star formation history, and Table 1 lists the best-fitting parameters. For a given IMF, star formation history, and set of stellar tracks the stellar masses are constrained to between $\pm$20% and $\pm$50%, similar to other published work in this field (Shapley et al. 2001, 2005; Förster Schreiber et al. 2004; Borys et al. 2005; Erb et al. 2006b, 2006c; Papovich et al. 2007). The stellar masses could be more uncertain if a large fraction of the stars were hidden behind a large amount of extinction such that the UV-IR SEDs are not sensitive to this component. While we cannot exclude such a scenario in the very dusty SMGs, we proceed in the following with the assumption that the SED fitting traces most of the stellar mass. Stellar masses range between 0.5 and 25 $\times$ 10^{10} $M_{\odot}$. Continuous star formation models or models with decay times $\geq$100 Myr are favored by the data for the SMGs and BzK/BX galaxies. The visual extinctions A_V range between 1 and 2 mag. Since the broadband photometry is dominated by the light from stars of all masses present in the galaxy, the star formation rates inferred from the stellar evolutionary modeling tend to represent past-averaged values in comparison to estimates of "instantaneous" star formation rates from Hα or the infrared luminosities, which are dominated by the most massive hot stars. Motivated by the (super)solar metallicity found from the R_{23} emission line analysis for SMM J140103+0252 (Tecza et al. 2004; cf. Nesvadba et al. 2007), we adopted solar metallicity tracks for the four SMGs. For the three $z \sim 2$ UV/optically selected star-forming galaxies the emission line ratios of Erb et al. (2006a, 2006b, 2006c), Förster Schreiber et al. (2006), and N. M. Förster Schreiber et al. (in preparation) suggest slightly subsolar metallicities (0.5–0.9 solar). We thus took stellar tracks

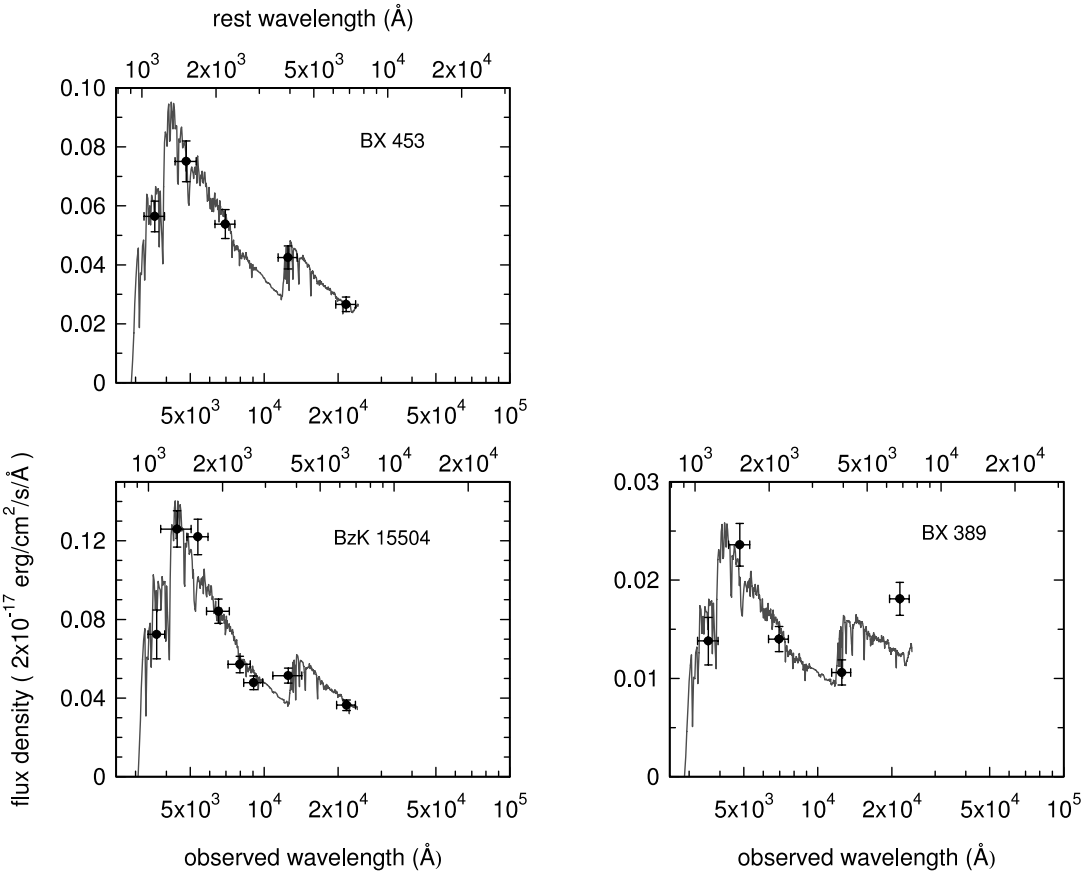

FIG. 7.—Rest-frame UV to optical spectral energy distributions of the three $z \sim 2$ UV/optically selected sources discussed in this paper, along with best-fitting constant star formation models and stellar ages, as discussed in the text. The photometric data points are from E. Daddi (2007, private communication) for BzK 15504 (see also supplementary material in Genzel et al. 2006), and from Erb et al. (2006c) for BX 453 and BX 389. The outlying *K*-band data point of BX 389 is probably a result of the contribution of Hα. Stellar masses quoted are for a Chabrier (2003) IMF and solar metallicity tracks; they include a correction for foreground extinction by the Milky Way. For the best-fitting star formation history parameters and masses see Table 1. [*See the electronic edition of the Journal for a color version of this figure*.]

of 0.5 and 1 times solar metallicities and averaged the results. For the $z \sim 3$ LBGs we used averages of the results for 0.2 and 0.5 solar metallicity tracks, as the emission line ratios suggest 0.3–0.5 times solar metallicity (Pettini et al. 2000; Smail et al. 2007; Coppin et al. 2007).

4.4. *Constraints on IMF, CO Conversion Factors, and Gas Fractions*

Table 1 summarizes the modeling inputs and results for all nine galaxies, including our best estimates of uncertainties. These latter

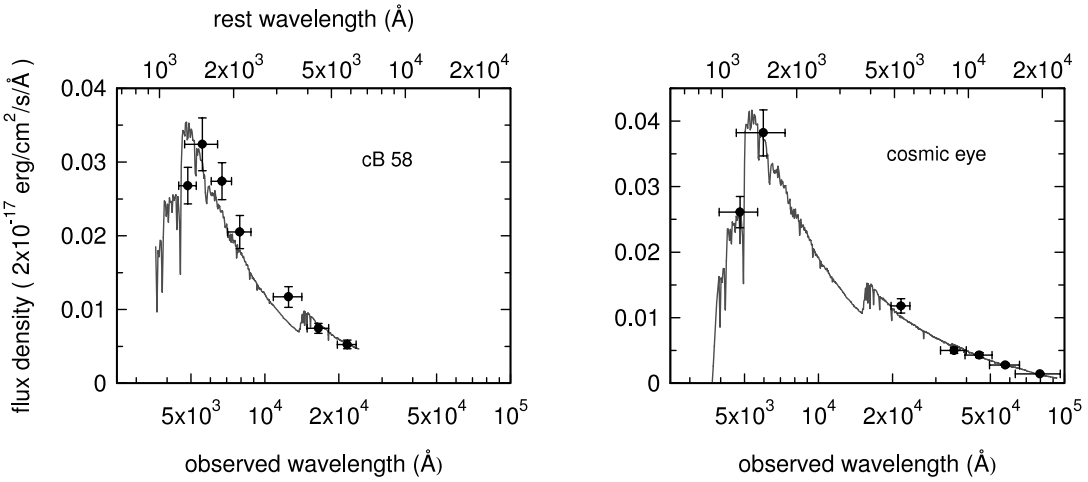

FIG. 8.—Rest-frame UV to near-infrared spectral energy distributions of the two lensed Lyman break galaxies discussed in this paper, along with best-fitting constant star formation models and stellar ages, as discussed in the text. The photometric data points are from Yee et al. (1996) and Ellingson et al. (1996) for cB58 and from Smail et al. (2007) and Coppin et al. (2007) for the Cosmic Eye. Stellar masses quoted are for a Chabrier (2003) IMF and 0.2 times solar metallicity tracks and include a correction for foreground extinction by the Milky Way and lensing magnification (factor 31.8 for cB58 and 28 for the Cosmic Eye). For the best-fitting star formation history parameters and masses see Table 1. [*See the electronic edition of the Journal for a color version of this figure*.]

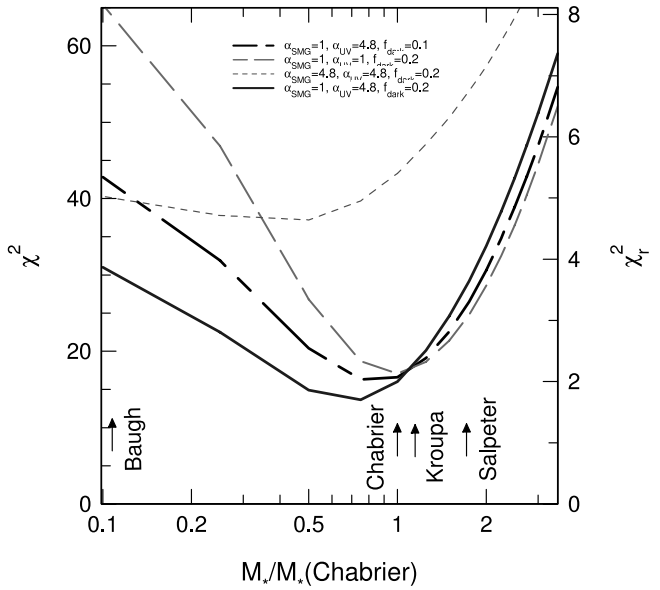

FIG. 9.—Dependence of $\chi^2 = \sum_i \{[M_{\rm dyn} - M_{\rm gas}(\alpha) - M_*({\rm IMF}) - M_{\rm dark}]/{\rm error}\}_i^2$ as a function of the IMF chosen (*horizontal scale*, in units of total M/L ratio, relative to the M/L ratio of a Kroupa [2001] IMF), for 9 $z \sim 2$–3 SMGs, sBzK/BX and LBGs with good constraints on dynamical masses $M_{\rm dyn}$, gas masses $M_{\rm gas}$ and stellar masses M_*. Here, $\chi^2_r = \chi^2/8$ is the reduced χ^2 value (*right vertical scale*). Continuous, dashed, dash-dotted, and dotted curves are for four different choices of the CO conversion factor α (in units of K km s^{-1} pc^2), and for a dark matter contribution of 10% and 20%, as annotated. In the χ^2 computation (eq. [3]), 2 σ limits to gas masses were treated as detections. [*See the electronic edition of the Journal for a color version of this figure.*]

are generally determined by various systematic effects and parameter correlations, especially between stellar masses and star formation histories/ages. We then calculated the global differences between dynamical masses and the sum of gas and stellar masses as a function of IMF and CO to gas conversion factors. We allowed for a contribution of dark matter within the $\leq$10 kpc radius of the star-forming disk/merger, $f_{\rm dark} = 0.1$–0.2, motivated by the findings in the local universe (Gerhard et al. 2001; Kassin et al. 2006). We computed in the usual manner the sample χ^2,

$$\chi^2 = \sum_{i=1}^{9} \left[\frac{M_{\rm dyn}(1 - f_{\rm dark}) - M_{\rm gas}(\alpha) - M_*(f_*)}{\sqrt{\delta M_{\rm dyn}^2 + \delta M_{\rm gas}^2 + \delta M_*^2}} \right]_i^2, \quad (4)$$

where the gas mass is a function of the adopted CO-gas conversion factor α, and the stellar mass is a function of $f_* = M_*/M_*$(Chabrier), the ratio of the stellar mass to that of a Chabrier IMF with the same rest-frame optical luminosity. The denominator contains the estimate of the uncertainty of each of these mass values. The sum of stellar, gas, and dark mass has to be equal to the dynamical mass. This means that for the appropriate IMF and α values, the numerator must be close to zero and the value of χ^2 in equation (3) close to the number of galaxies (=9). Hence the best values for α and f_* can in principle deduced by minimizing χ^2 as a function of these two parameters.

Figure 9 shows the resulting χ^2 distribution as a function of f_* and for different plausible values of α and $f_{\rm dark}$. While the results clearly still have large statistical and systematic uncertainties, this new method appears quite promising and delivers interesting initial constraints.

1. For all plausible choices of the CO-to-gas conversion factors, the χ^2 minimum lies between $f_* \sim 0.75$ and 1.05, in good agreement with a "universal" Kroupa or Chabrier IMF. Formally, the lowest minimum is achieved for $f_* = 0.75$, perhaps indicating an IMF that is somewhat shallower or more top-heavy than a Chabrier/Kroupa IMF. Including a range of $\delta\chi^2 = \pm 2$ from these minima we find that f_* must lie between 0.5 and 1.3. A 0.1–100 Salpeter IMF ($f_* \sim 1.7$) as well as extreme top-heavy IMFs applicable over the total star formation histories of these galaxies appear to be excluded by our data.

2. A Galactic conversion factor for all nine sources ($\alpha_{\rm SMG} = \alpha_{\rm UV/optical} = 4.8$) is strongly disfavored, as it leads to an overestimate of the dynamical masses for all stellar mass functions and thus to very poor χ^2 values.

3. A ULIRG conversion factor ($\alpha_{\rm SMG} = \alpha_{\rm UV/optical} \sim 1$) for both SMGs and UV/optically selected galaxies is possible in terms of our χ^2 analysis. However, this choice would imply gas fractions of only a few percent on average in the BX/BzK/LBG galaxies we have observed. In that case we would have to be observing all these sources at the time when they are about to run out of gas. This appears very improbable and is also inconsistent with the finding of Daddi et al. (2007) that the dispersion of the luminosities/star formation rates of sBzKs at a given stellar mass is fairly small, implying that the star formation process in these galaxies is steady and has a high duty cycle.

4. The lowest χ^2 values are obtained for a combination of CO-to-gas conversion factors similar to those favored in the local universe, for instance $\alpha_{\rm SMG} = 1\ M_\odot$ (K km s^{-1} pc^2)$^{-1}$ (corresponds to $\alpha/\alpha_{\rm G} = 0.2$), similar to what is found for local ULIRGs, and $\alpha_{\rm UV/optical} = 4.8$ ($\alpha/\alpha_{\rm G} \sim 1$).

5. With this selection of conversion factors the gas fractions of UV/optically selected and submillimeter galaxies appear to be quite similar, which would be the intuitive guess based on their gas and star formation surface densities in the context of a Schmidt-Kennicutt star formation recipe (Bouché et al. 2007). The inferred average gas fractions are $\sim$30% for the SMGs, $\sim$50% for the LBGs and $\leq$20% for the sBzK/BX galaxies we have observed.

6. A Perhaps surprising result emerging from the fitting of the four SMGs is the relatively old stellar ages (0.64–2.5 Gyr) deduced in the framework of the continuous star formation model. Borys et al. (2005) have likewise found $\sim$2 Gyr ages for their sample of 11 HDF-N galaxies (HDF 76 and HDF 242 were common between the two studies). These values are comparable to the average ages of the sBzK population (Daddi et al. 2007) and the $K \leq 20$ BX population (Shapley et al. 2004; Erb et al. 2006b, 2006c). The specific values deduced, however, depend on the assumptions about the star formation histories. For exponential decay "burst" models, ages are lower (a few hundred Myr), but such models in turn lead to larger discrepancies between the current star formation rates deduced from these models and the instantaneous star formation rates inferred from the submillimeter flux densities.

Our conclusions necessarily need to be considered with caution, because of the small sample of sources, the large uncertainties, and the assumptions that went into our analysis. For instance we assumed that there is a single IMF for both the strongly bursting (SMG) as well as the more quiescently star-forming stellar components and that both have approximately the same extinction. However, if bursting and quiescent star formation modes have different IMFs (as assumed by Baugh et al. 2005), and/or if the obscuration of the stars powering the far-infrared luminosity is sufficiently large, a top-heavy IMF could still be compatible with the burst component. Another area of concern is the accuracy of the stellar masses obtained from SED fitting. While the statistical

TABLE 2
COMOVING VOLUME DENSITIES OF DIFFERENT $z \sim 1$–3.4 GALAXY SAMPLES

Galaxy Sample	Φ (h_{70}^3 Mpc^{-3})
Submillimeter galaxies (SMGs): $S_{850\,\mu m} \geq 5$ mJy, $z = 1$–3.4	$1.1 \pm 0.1 \times 10^{-5}$[a]
Optically faint radio galaxies OFRGs: $z = 1$–3.4	$\sim 1 \times 10^{-5}$[a]
BX/BM, $K \leq 20$, $z = 1.4$–2.5	$1.1 \pm 0.3 \times 10^{-4}$[b,d]
Star-forming, $K \leq 20$ BzK, $z = 1.4$–2.6	$2.2 \pm 0.6 \times 10^{-4}$[b,c,d]
Star-forming, $K \leq 20$ DRG, $z = 2.0$–2.6	7.5×10^{-5}[b]
Star-forming, $K \leq 21.7$ DRG, $z = 2.0$–2.6	$12 \pm 3 \times 10^{-4}$[b,e]
Quiescent (passive), $K \leq 20$ BzK, $z = 1.4$–2	$1.5 \pm 0.4 \times 10^{-4}$[b,c,d]
Quiescent (passive), $K \leq 21.7$ DRG, $z = 2.0$–2.6	$6.5 \pm 2 \times 10^{-4}$[b,e]

[a] Chapman et al. (2005).
[b] Reddy et al. (2005), GOODS-N.
[c] Daddi et al. (2004a, 2004b, 2005), Kong et al. (2006), GOODS-S, HUDF, Deep 3a, Daddi-F.
[d] Grazian et al. (2007), MUSIC.
[e] Zirm et al. (2007), Toft et al. (2007), HDF-S, MS1054.

errors can be reasonably well estimated with the methods we have applied, the inherent uncertainties in the input stellar models (notwithstanding recent improvements, see above), star formation histories, and dust extinction of different stellar components are much harder to quantify and certainly would tend to increase our error bars. A final unknown is the fraction of dark matter in the central few kpc of the galaxies we studied. With these caveats in mind the current evidence supports a near universal (=Galactic) IMF in the z$\sim$2 star-forming galaxies we have observed, in excellent agreement with the discussion of Renzini (2005). Our measurements also favor ^{12}CO to gas mass conversion factors that are dependent on ISM gas surface density $\Sigma_{\rm gas}$ [and thus on gas pressure $P \sim (\Sigma_{\rm gas})^2$] and on metallicity. Obviously an extension of our "dynamical" method to a larger sample of galaxies, and including more systems with good rotation curves to constrain baryonic and dark matter contributions would be highly desirable.

5. DISCUSSION AND CONCLUSIONS

We have presented in this paper $<0.5''$ FWHM millimeter interferometry observations of four $z \sim 2$ SMGs and strict limits to the CO fluxes of three UV/optically selected $z \sim 2$ galaxies. We have spatially resolved the kinematic structure in the former set of compact, powerful star-forming galaxies. We find strong dynamical evidence for major dissipative merging. Velocity fields are complex and chaotic, and there are interacting double systems. Several SMGs have low angular momentum gas disks. Our data thus add compelling empirical evidence in favor of previous arguments (e.g., Smail et al. 2002, 2005; Greve et al. 2005; Swinbank et al. 2006; Tacconi et al. 2006) that SMGs are short-duration maximum starburst events in the evolution of a major, gas-rich (>30% gas fraction) merger of massive galaxies. But how long do these SMG events last?

We can constrain the duration and duty cycle of the SMG phase in two ways. First, we can make a quantitative estimate of the duration of the starburst phase of these objects from the ratio of the cosmic volume density of SMGs and that of the quiescent population in the same mass and redshift ranges, as the latter are plausibly the descendants of the former (§ 3.1). Table 2 shows a comparison of the cosmic comoving volume densities of the different samples taken from the recent literature. The quiescent objects are highly clustered (Kong et al. 2006), resulting in large cosmic variance. The volume densities listed in Table 2 are derived from observations in a number of fields, however, so that the amplitude of the cosmic variance should be reduced, which is reflected in the error bars quoted in Table 2. Comparing the density of $K \leq 20$ objects to the SMGs, we estimate the SMG "duty cycle" to be $\eta_{\rm SMG} \sim 7\%$. This is justified for two reasons. First, a selection of passive galaxies to this limit picks galaxies with $M_* \geq 10^{11}\ M_\odot$, similar to the stellar mass of $S_{850\,\mu m} \geq 5$ mJy SMGs (Smail et al. 2004; Borys et al. 2005; Table 1). Second, the clustering correlation length of $S_{850\,\mu m} \geq 5$ mJy SMGs is $6.9 \pm 2.1\ h^{-1}$ Mpc (Blain et al. 2004), in good agreement with the clustering correlation length of $K \leq 20$ qBzKs (Kong et al. 2006; E. Daddi et al., in preparation). If one adds in addition to SMGs the sample of optically faint radio galaxies in the same $z \sim 2$–3 redshift range, which plausibly are gas-rich major mergers of somewhat hotter dust temperature but otherwise of star formation rate and mass comparable to those of the $S_{850\,\mu m} \geq 5$ mJy SMGs (Chapman et al. 2004; Smail et al. 2004), $\eta_{\rm SMG}$ would go up by a factor of 2 or so. On the other hand, if one compares to qDRGs to $K \leq 21.7$, $\eta_{\rm SMG}$ would be lower by a factor of 2–4, depending what fraction of these systems still is in the same mass range as the SMGs. We conclude that a plausible estimate of the duty cycle of $M \sim 10^{11}\ M_\odot$ major merger induced starbursts is $\eta_{\rm SMG} \sim 10\%$, with an uncertainty of a factor of 2 in both directions. Over the $\sim$1–1.5 Gyr duration of the cosmic epoch considered here this translates into a duration of the SMG phase of 100–150 Myr, or 50–300 Myr taking into account the uncertainties.

A second, independent estimate of the SMG duty cycle comes from the comparison of stellar ages and gas exhaustion timescales. From the gas masses and instantaneous star formation rates (from submillimeter fluxes) in Table 1 we compute the current gas exhaustion timescales, $t_{\rm exh} \sim 2M_{\rm gas}/{\rm SFR}$ (col. [12] in Table 1). We then infer the duty cycle η_* of the current star formation activity from $\eta_* = 2t_{\rm exh}/t_*$, where t_* is the age of the stellar population inferred from our SED modeling (col. [11] in Table 1), and the factor 2 takes into account in an average sense the "previous" star formation history. With the CO-H_2 conversion factors discussed in § 4.4 we find $\eta_*({\rm SMG}) \sim 0.1$. Allowing for additional gas accretion after the current SMG event would increase the gas reservoir, and thus also η_*. The estimates of the SMG duty cycle based on volume densities and gas exhaustion timescales thus are in good agreement with each other, and also with earlier estimates (Tecza et al. 2004; Smail et al. 2004; Chapman et al. 2005; Greve et al. 2005; Swinbank et al. 2006). The same considerations indicate much larger duty cycles for the UV/optically selected $z \sim 2$ galaxies in our sample [$\eta_*({\rm sBzK/BX}) \leq 0.75$ and $\eta_*({\rm LBG}) \sim 1$]. This is in agreement

with Daddi et al. (2007), who find a relatively small scatter of the star formation rate to stellar mass ratio of $z \sim 1.5$–2.5 sBzKs, implying that star formation in sBzKs is fairly steady (see also Noeske et al. [2007] for a similar conclusion at $z \sim 1$). The short duration of the SMG phase likely results from the combined requirements of triggering such a "maximum starburst" (Tacconi et al. 2006) and terminating it owing to negative feedback from supernova and AGN activity (Chapman et al. 2005). The $\sim$100 Myr total duration is also broadly consistent with the duration of pericenter passage compressions and the final merger phase of a dissipative major merger at $z \sim 2$ (Mihos & Hernquist 1994, 1996; Barnes & Hernquist 1996; Hopkins et al. 2006; Chakrabarti et al. 2007). Keeping in mind the large uncertainties in model parameters, extinction corrections, IMF, etc., we propose that a significant fraction ($\sim$50%) of the stellar mass of these $\sim M_*$ galaxies formed and assembled in the most active phases of a single gas-rich, major merger event, while the rest formed over a longer period of time (>1 Gyr), both during as well as before the merger. In that case, one would naturally expect a significant fraction of those SMGs that are not in the submillimeter bright state but have not yet lost most of their gas to be present in the sBzK/DRG/BX samples, in agreement with Reddy et al. (2005). They may be similar to other sBzK/DRG/BX galaxies in terms of mass and star formation rate but recognizable as "mergers" in terms of disturbed kinematics and gas distributions.

The observations presented above add new information on the formation and evolution of massive spheroids. If the properties of the small SMG sample we have studied so far are typical for the SMG population as a whole, we have found the smoking gun for an (or possibly the most) important creation process of spheroids at high redshift: a major and highly dissipative, "wet" merger of very gas-rich galaxies, leading to rapid and efficient star formation and compact merger remnant formation. This conclusion is not surprising. A merger origin of the SMG phenomenon has been favored for some time (e.g., Smail et al. 1998, 2004; Chapman et al. 2004; Khochfar & Silk 2006; Cimatti et al. 2008). Our data, however, provide clear-cut evidence for this assumption (see also Swinbank et al. 2006). Our SMG data also support other emerging evidence from high-resolution optical observations that many or most of the massive spheroids at $z \sim 1.4$–2.5 are much more compact and dense than $z \sim 0$ spheroids (Daddi et al. 2005; Zirm et al. 2007; Toft et al. 2007; Trujillo et al. 2007, 2008). Cimatti et al. (2008) conclude from the first spectroscopic data for $z \sim 1.5$ qBzKs that their stellar ages are about 1 Gyr, consistent with a formation redshift of $z \sim 2$–3. What becomes of the merger remnants between $z \sim 2$ and 0? To connect the $z \sim 2$ location of the SMGs/qDRGs/qBzKs to the $z \sim 0$ spheroid track, the further evolutionary path has to proceed from high density to low density (Fig. 7). Dry major mergers would appear to be a natural choice (van Dokkum 2005; Bell et al. 2006; Naab et al. 2006; Boylan-Kolchin et al. 2006). The dry merger track (red arrow on the right of Fig. 5; Nipoti et al. 2003) connects the locus of the $z \sim 2$ remnants to the most massive cluster ellipticals at $z \sim 0$ at a mass of $M_* \geq 10^{12}\ M_\odot$. The $z = 0$ comoving volume density of dark halos with the appropriate mass for such clusters ($\sim 10^{14}\ M_\odot$) is $\sim 2.5 \times 10^{-5}\ h_{0.7}^3\ \mathrm{Mpc}^{-3}$ (Mo & White 2002), sufficiently large to be consistent with the hypothesis that every SMG at $z \sim 2$–3 becomes a massive cluster elliptical.

However, in the most simple version of dry major mergers, the dense central regions of the original compact high-z remnants would have to still be observable at $z \sim 0$, in contradiction with the inward extrapolation of a Hernquist (1990) model for a very massive $z \sim 0$ remnant that could be the end result of this process (dotted curves in the right inset of Fig. 5). In addition, S. Genel et al. (in preparation) have carried out an analysis of the Millennium dark matter simulation (Springel et al. 2005), which indicates that a halo of mass $\sim 10^{12}$–$10^{13}\ M_\odot$, appropriate for a SMG, experiences on average only $\sim$1 major merger between $z \sim 2.5$ and 0, and only $\sim$8% of these halos experience three or more major mergers in this redshift interval. This major merger rate is not sufficient to account for the required factor $\sim$5–10 mass increase from the $z \sim 2$ SMGs/qBzKs/qDRGs onto the $z = 0$ spheroid track. Finally, Burkert (2008) conclude from the structure/dynamics of massive and boxy, $z \sim 0$ spheroids in the SAURON sample that their properties cannot be accounted for solely by major dry mergers but more probably require a sequence of major *and minor* mergers. Further detailed simulations are needed to settle the question whether a combination of dry major mergers, minor mergers as well as smooth accretion lead to the observed properties of very massive local ellipticals (Cox et al. 2006; Boylan-Kolchin et al. 2006; Naab et al. 2007).

Another possibility is that the compactness of the $z \sim 2$ SMG/qBzK/qDRG population is misleading in terms of their overall stellar mass distribution. In reality there may be a bright central starburst region dominating the surface brightness distribution, which is surrounded by a much larger halo of older stars dominating the overall mass distribution (e.g., Daddi et al. 2005). As discussed by Tacconi et al. (2002) in the context of compact $z \sim 0$ ULIRG merger remnants, the half-light radius of such a configuration would be expected to significantly increase over a few Gyr, as initially the most massive OB stars (dominating the dust/CO emission) and then the bright TP-AGB stars (dominating the qBzK/qDRG phase) in the central starburst fade over time. This effect obviously would lessen the discrepancy between the half-light densities of the $z \sim 2$ and 0 spheroids.

We thank the staff of the IRAM Observatory for their support of this program. We are grateful to Thorsten Naab, Andi Burkert, and Amiel Sternberg for valuable discussions. We also thank the referee for constructive comments that have helped to clarify and improve the paper. I. R. S. acknowledges support from the Royal Society, and A. M. S. acknowledges support from STFC.

APPENDIX A

THE CO TO H_2 CONVERSION FACTOR

More than 30 years of molecular line observations in giant molecular clouds of the Milky Way have established that the integrated line flux of ^{12}CO millimeter rotational lines can be used to infer gas masses, despite the facts that the CO molecule only makes up a small fraction of the entire gas mass and that the lower rotational lines (1–0, 2–1, and 3–2) are almost always very optically thick (Solomon et al. 1987, and references therein). This result stems from the fact that CO emission in the Milky Way and nearby normal galaxies comes from moderately dense [volume-averaged densities $\langle n(\mathrm{H_2}) \rangle \sim 200\ \mathrm{cm}^{-3}$], virialized (i.e., self-gravitating) giant

molecular clouds (GMCs). In this regime it can be shown (Dickman et al. 1986; Solomon et al. 1987; Solomon & Barrett 1991) that the ratio of H_2 column density to CO flux I_{CO} [$I_{CO} = \int_{line} T_R(v)\,dv$], or gas mass (including a 36% mass correction for helium) to CO luminosity L'_{CO} [$L'_{CO} = \int_{source}\int_{line} T_R(v)\,dv\,dA$] can be expressed as

$$\frac{N(H_2)}{I(CO)} = X = c_1\left(\frac{\langle n(H_2)\rangle}{200\ \mathrm{cm^{-2}}}\right)^{1/2}\left(\frac{T_R}{6\ \mathrm{K}}\right)^{-1}\ \left[\mathrm{cm^{-2}/(K\ km\ s^{-1})}\right], \tag{A1}$$

$$\frac{M_{gas}}{L'_{CO}} = \alpha = c_2\left(\frac{\langle n(H_2)\rangle}{200\ \mathrm{cm^{-2}}}\right)^{1/2}\left(\frac{T_R}{6\ \mathrm{K}}\right)^{-1}\ \left[M_\odot/\mathrm{(K\ km\ s^{-1}pc^2)}\right], \tag{A2}$$

where T_R is the equivalent Rayleigh-Jeans brightness temperature of the (optically thick) CO line and c_1 and c_2 are appropriate numerical constants. In the 2.6 mm CO(1–0) transition the typical gas temperature of Galactic GMCs is ~8–10 K. For spherical clouds supported by isotropic random motions (e.g., turbulence) in virial equilibrium with their own gravity, the resulting inferred theoretical conversion factors are $X \sim 2\times10^{20}$ [$\mathrm{cm^{-2}\ (K\ km\ s^{-1})^{-1}}$] and $\alpha = 4.3$ [$M_\odot$ (K km s^{-1} pc^2)$^{-1}$]. Several independent empirical techniques based on GeV γ-rays, optical extinction measurements, isotopomeric line ratios, and excitation analysis have all shown that this "virial" technique is appropriate and remarkably robust throughout the Milky Way (Strong & Mattox 1996; Dame et al. 2001; Dickman et al. 1986; Solomon et al. 1987). The "standard" empirical conversion factor X_G ranges between 2 and 3×10^{20} (left filled circle in Fig. 10). In the following we adopt $X_G = 2.2\times10^{20}$ and $\alpha_G = 4.8$. The validity of this simple proportionality is surprising, as it implies that average densities and temperatures vary little across the Milky Way clouds, or only in a way that the ratio of $n(H_2)^{1/2}/T$ is constant.

Dickman et al. (1986) have extended the virial approach to external galaxies by showing that equations (A1) and (A2) apply even when one is observing an ensemble of virialized clouds, instead of a single one, as long as again the factor $n(H_2)^{1/2}/T$ is constant throughout the system and the CO line is optically thick. This assumption of an ensemble of individual gas clouds in virial equilibrium with their own gravity breaks down, however, in galactic nuclei and starburst galaxies. Gas motions there are due to a combination of gas and stellar mass components, and the gas is often in a smoother, disklike configuration. Downes et al. (1993), Solomon

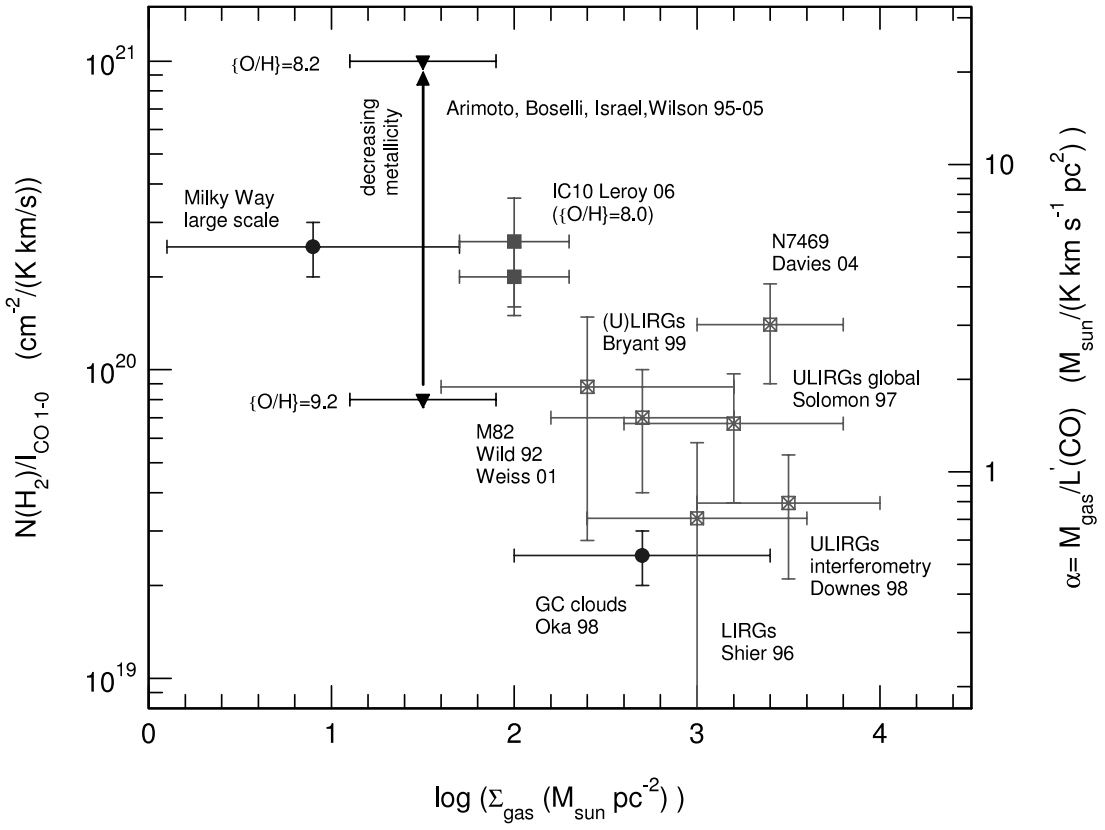

FIG. 10.—Compilation of the conversion factor X from CO(1–0) flux [I_{CO} (K km s^{-1})] or luminosity [L'_{CO} (K km s^{-1} pc^2)] to H_2 column density (*left vertical scale*) and total (H_2 + He ı) gas mass (*right vertical scale*), derived in various $z \sim 0$ Galactic and extragalactic targets. Filled circles denote measurements in the disk and center of the Milky Way, based on various virial, extinction, and isotopomeric analyses (Solomon et al. 1987; Strong & Mattox 1996; Dame et al. 2001; Oka et al. 1998). Crossed squares denote measurements in starbursts and (U)LIRGs, mainly based on dynamical constraints (Wild et al. 1992; Davies et al. 2004; Shier et al. 1994; Hinz & Rieke 2006; Weiss et al. 2001; Solomon et al. 1997; Downes & Solomon 1998; Bryant & Scoville 1999). Filled triangles denote conversion factors as a function of decreasing metallicity (*vertical arrow*) from {O/H} = 12 + [O/H] = 9.2 (*bottom*) to 8.2 (*top*), derived mainly from global (large scale) dust mass measurements in nearby galaxies and dwarfs by several groups (Arimoto et al. 1996; Israel 2000, 2005; Boselli et al. 2002; see also Wilson 1995). In contrast, filled squares mark X-factor measurements toward individual clouds, over the same range in metallicity (Rosolowsky et al. 2003; Leroy et al. 2006). [*See the electronic edition of the Journal for a color version of this figure.*]

et al. (1997), and Downes & Solomon (1998) have shown that in this limit equations (A1) and (A2) still apply but in a slightly modified form

$$\frac{N(\mathrm{H_2})}{I(\mathrm{CO})} = X = c_3 f_{\mathrm{gas}}^{1/2} \left(\frac{H/R}{0.15}\right)^{1/2} \left(\frac{\langle n(\mathrm{H_2})\rangle}{200\ \mathrm{cm^{-2}}}\right)^{1/2} \left(\frac{T_{\mathrm{R}}}{6\ \mathrm{K}}\right)^{-1} \left[\mathrm{cm^{-2}}/\left(\mathrm{K\ km\ s^{-1}}\right)\right], \tag{A3}$$

$$\frac{M_{\mathrm{gas}}}{L'_{\mathrm{CO}}} = \alpha = c_4 f_{\mathrm{gas}}^{1/2} \left(\frac{H/R}{0.15}\right)^{1/2} \left(\frac{\langle n(\mathrm{H_2})\rangle}{200\ \mathrm{cm^{-2}}}\right)^{1/2} \left(\frac{T_{\mathrm{R}}}{6\ \mathrm{K}}\right)^{-1} \left[M_\odot/\left(\mathrm{K\ km\ s^{-1}pc^2}\right)\right], \tag{A4}$$

where f_{gas} is the mass fraction of gas in the galaxy, H/R is the ratio of vertical height and radius of the gas layer, and c_3 and c_4 are numerical constants. For conditions appropriate for luminous or ultraluminous infrared galaxies [(U)LIRGs: $n(\mathrm{H_2}) \sim 10^3$–$10^4$ cm^{-3} and $T_{\mathrm{R}} \sim 20$–50 K] with $H/R = 0.15$–0.2 and $f_{\mathrm{gas}} \sim 0.1$–0.3, the inferred theoretical conversion factors range between $\alpha = 0.8$ and 1.6 ($X = 3.7$–7.3×10^{19}: Solomon et al. 1997; Downes & Solomon 1998). Again, various empirical calibrations of the X/α factors in the Galactic center, nearby AGN and (U)LIRGs, based on dynamical mass measurements, are in good agreement with these theoretical considerations. Figure 10 shows an (incomplete) compilation of a number of these X-factor determinations in the literature. Since in the context of the "Schmidt-Kennicutt" (Kennicutt 1998) empirical relation star formation surface density scales with gas surface density it is appropriate to plot, as in Figure 10, the derived X-factors as a function of Σ_{gas} ($M_\odot$ pc^{-2}). These measurements (crossed squares and the bottom filled circle for clouds in the Milky Way center) suggest that in dense environments ($\Sigma_{\mathrm{gas}} \sim 10^{2.5}$–$10^4$ $M_\odot$ pc^{-2}) the conversion factor is 0.2–0.5 times the value in the extended GMC population of the Milky Way disk.

Another important variable is the metallicity of the gas. The above discussion relates to near- or supersolar metallicity environments in moderately massive $z \sim 0$ galaxies. Using calibrations based mainly on optically thin far-infrared/submillimeter dust emission and isotopomeric line measurements several groups have found that the global conversion factor in nearby galaxies appears to be a strong function of metallicity (Arimoto et al. 1996; Israel 2000, 2005; Boselli et al. 2002). The average of these results gives the following relationship between X-factor and oxygen abundance

$$\log(X) = 29.2 - (12 + \{\mathrm{O/H}\}). \tag{A5}$$

This relationship is plotted in Figure 10 as filled triangles for oxygen abundances of 9.2 (*bottom*) and 8.2 (*top*); the arrow connects these extreme values.

Rosolowsky et al. (2003) and Leroy et al. (2006) have derived X-factors from high-resolution, virial measurements toward individual dense GMCs in nearby galaxies over the same range in metallicity as discussed above. These measurements indicate only a weak metallicity dependence of the X-factor (filled squares in Fig. 10). This is in contrast to and probably superseding earlier interferometric measurements by Wilson (1995) that did show a trend similar to equation (A5).

This situation is confusing. However, the contradiction may be qualitatively understood and resolved in terms of the physics of photodissociation regions (e.g., Israel 2000). In star-forming galaxies the optically thick CO lines (1–0, 2–1, 3–2, etc.) come from the surface layers of GMCs that are exposed to and heated by the local far-UV radiation field (Wolfire et al. 1993). Far-UV radiation also dissociates CO molecules, but in solar metallicity environments, dust shielding and CO self-shielding are efficient enough that only a moderately thin (∼10%) surface layer is dissociated where carbon is then in the form of C II AND C I. At lower metallicities, dust and CO self-shielding is correspondingly less efficient. For instance, for $Z \sim 0.25\ Z_\odot$ UV radiation dissociates 6–10 times deeper in terms of overall hydrogen column density than at solar metallicity, while the much more effective H_2 self-shielding leaves the H_2 column basically unaffected (Maloney & Black 1988; Maloney & Wolfire 1997). In dense enough clouds, the remaining CO column is typically still sufficiently large to make the lower rotation transitions of ^{12}CO optically thick, resulting in similar conversion factors as in higher metallicity environments. For the more diffuse molecular gas the situation may be drastically different, however, leading to a situation that the effective filling factor of CO-emitting gas is much less than that of H_2 (Israel 2000). These considerations may explain the difference between the interferometric measurements of Rosolowsky et al. (2003) and Leroy et al. (2006) and the global measurements of Arimoto, Israel, Boselli, and others. They are also consistent with the far-infrared observations of the [C II] 158 μm line by Madden et al. (1997), who infer the presence of molecular gas without CO emission in the $Z \sim 0.25\ Z_\odot$ galaxy IC10.

How are the values in Figure 10 to be extrapolated to high redshift and what conversion factors are likely applicable to SMGs or UV/optically selected $z \sim 2$–3 star-forming galaxies? Optical emission line ratios [F([N II])/F(Hα), $R_{23} = [F(\mathrm{O\ III}) + F(\mathrm{O\ II})]/F(\mathrm{H}\beta)$] suggest that the high-mass end ($K < 20$) of the UV/optically selected $z \sim 2$ star-forming galaxies ($M_* \sim 10^{11}\ M_\odot$), including BX 389, BX 453, and BzK 15504 in Table 1, have ionized gas phase metallicities close to but somewhat below solar [$(12 + \{\mathrm{O/H}\}) \sim 8.4$–8.6; Erb et al. 2006a; Shapley et al. 2004; N. M. Förster Schreiber et al., in preparation]. The metallicities of the $z \sim 3$ LBGs are lower (Pettini et al. 2001). For cB58 Pettini et al. (2000) find $(12 + \{\mathrm{O/H}\} \sim 8.1)$. BzK 15504 (Genzel et al. 2006) and BX 389 (Förster Schreiber et al. 2006) are rotating disks with large, self-gravitating gas complexes, so that equations (A1) and (2) are probably appropriate. For the more dispersion dominated sources BX 453, and perhaps cB58 (Baker et al. 2004) and the "Cosmic Eye" (Coppin et al. 2007) as well, both sets of equations (A1)/(2) and (A3)/(4) may be appropriate (see discussion in Coppin et al. 2007). Typical gas volume and surface densities of Galactic molecular clouds are $10^{2.5}$ cm^{-3} and $10^{2.5}\ M_\odot$ pc^{-2}, and gas temperatures may be 20–30 K. From these considerations we conclude that for BX 389, BX 453, and BzK 15504 a conversion factor of $\alpha/\alpha_{\mathrm{G}} \sim 1$ is a plausible guess. Given their lower metallicities, the LBGs may have $\alpha/\alpha_{\mathrm{G}} \sim 1$–3 (see Baker et al. 2004). The SMGs are scaled-up, and more gas-rich versions of local ULIRGs (Tacconi et al. 2006; Greve et al. 2005), with average molecular gas densities of $>10^3$ cm^{-3}, gas surface densities $>10^3$–$10^4\ M_\odot$ pc^{-2} and gas temperatures of 30–40 K. In the case of SMG 14011+0252 J1 at $z = 2.56$, Tecza et al. (2004) find $(12 + \{\mathrm{O/H}\}) = 8.92 \pm 0.07$ from the R_{23} metallicity estimator, significantly supersolar. If these values are representative for the SMGs as a whole, as may be suggested by the [N II]/Hα line ratios found by Swinbank et al. (2004), an appropriate conversion factor is $\alpha/\alpha_{\mathrm{G}} \sim 0.2$–0.5, similar to the values for local starbursts and ULIRGs in Figure 10.

REFERENCES

Adelberger, K. L., Steidel, C. C., Shapley, A. E., Hunt, M. P., Erb, D. K., Reddy, N. A., & Pettini, M. 2004, ApJ, 607, 226
Arimoto, N., Sofue, Y., & Tsujimoto, T. 1996, PASJ, 48, 275
Baker, A., Tacconi, L. J., Genzel, R., Lehnert, M. D., & Lutz, D. 2004, ApJ, 604, 125
Barnes, J. E., & Hernquist, L. 1996, ApJ, 471, 115
Baugh, C. M., Lacey, C. G., Frenk, C. S., Granato, G. L., Silva, L., Bressan, A., Benson, A. J., & Cole, S. 2005, MNRAS, 356, 1191
Bell, E., et al. 2006, ApJ, 640, 241
Biggs, A. D. & Ivison, R. J. 2008, MNRAS, 385, 893
Blain, A. W., Chapman, S. C., Smail, I. R., & Ivison, R. J. 2004, ApJ, 611, 725
Blain, A. W., Smail, I., Ivison, R. J., Kneib, J.-P., & Frayer, D. T. 2002, Phys. Rep., 369, 111
Borys, C., Smail, I., Chapman, S. C., Blain, A. W., Alexander, D. M., & Ivison, R. J. 2005, ApJ, 635, 853
Boselli, A., Lequeux, J., & Gavazzi, G. 2002, Ap&SS, 281, 127
Bouché, N., et al. 2007, ApJ, 671, 303
Boylan-Kolchin, M., Ma, C.-P., & Quataert, E. 2006, MNRAS, 369, 1081
Bruzual, G. 2007, in ASP Conf. Ser. 374, From Stars to Galaxies: Building the Pieces to Build Up the Universe, ed. A. Vallenari et al. (San Francisco: ASP), 303
Bruzual, G., & Charlot, S. 2003, MNRAS, 344, 1000
Bryant, P. M., & Scoville, N. Z. 1999, AJ, 117, 2632
Burkert, A., Naab, T. & Johansson, P.H. 2007, ApJ, submitted (arXiv: 0710.0663)
Calzetti, D., Armus, L., Bohlin, R. C., Kinney, A. L., Koorneef, J., & Storchi-Bergmann, T. 2000, ApJ, 533, 682
Carilli, C. L., & Wang, R. 2006, AJ, 131, 2763
Chabrier, G. 2003, PASP, 115, 763
Chakrabarti, S., Cox, T. J., Hernquist, L., Hopkins, P., Robertson, B., & di Matteo, T. 2007, ApJ, 658, 840
Chapman, S. C., Blain, A. W., Ivison, R. J., & Smail, I. R. 2003, Nature, 422, 695
Chapman, S. C., Blain, A. W., Smail, I. R., & Ivison, R. J. 2005, ApJ, 622, 772
Chapman, S. C., Smail, I. R., Windhorst, R., Muxlow, T., & Ivison, R. J. 2004, ApJ, 611, 732
Cimatti, A., et al. 2008, A&A, 482, 21
———. 2007, ApJ, 665, 936
Cox, T. J., Dutta, S. N., di Matteo, T., Hernquist, L., Hopkins, P. F., Robertson, B., & Springel, V. 2006, ApJ, 650, 791
Daddi, E., Cimatti, A., Renzini, A., Fontana, A., Mignoli, M., Pozetti, L., Tozzi, P., & Zamorani, G. 2004a, ApJ, 617, 746
Daddi, E., et al. 2004a, ApJ, 600, L127
———. 2005, ApJ, 626, 680
———. 2007, ApJ, 670, 156
———. 2008, ApJ, 673, L21
Dame, T. M., Hartmann, D., & Thaddeus, P. 2001, ApJ, 547, 792
Dasyra, K. M., et al. 2006, ApJ, 638, 745
Davé, R. 2008, MNRAS, 385, 147
Davies, R., Tacconi, L. J., & Genzel, R. 2004, ApJ, 602, 148
Dickman, R. L., Snell, R. L., & Schloerb, P. F. 1986, ApJ, 309, 326
Downes, D., & Eckart, A. 2007, A&A, 468, L57
Downes, D., & Solomon, P. M. 1998, ApJ, 507, 615
———. 2003, ApJ, 582, 37
Downes, D., Solomon, P. M., & Radford, S. J. E. 1993, ApJ, 414, L13
Ellingson, E., Yee, H. K. C., Bechtold, J., Elston, R., & Carlberg, R. G. 1996, JRASC, 90, 313
Erb, D. K., Shapley, A. E., Pettini, M., Steidel, C. C., Reddy, N. A., & Adelberger, K. L. 2006a, ApJ, 644, 813
Erb, D. K., Steidel, C. C., Shapley, A. E., Pettini, M., Reddy, N. A., & Adelberger, K. L. 2006b, ApJ, 646, 107
———. 2006c, ApJ, 647, 128
Förster Schreiber, N. M., Genzel, R., Lutz, D., Kunze, D., & Sternberg, A. 2001, ApJ, 552, 544
Förster Schreiber, N. M., et al. 2004, ApJ, 616, 40
———. 2006, ApJ, 645, 1062
Franx, M., et al. 2003, ApJ, 587, L79
Genzel, R., Baker, A. J., Tacconi, L. J., Lutz, D., Cox, P., Guilloteau, S., & Omont, A. 2003, ApJ, 584, 633
Genzel, R., Tacconi, L. J., Rigopoulou, D., Lutz, D., & Tecza, M. 2001, ApJ, 563, 527
Genzel, R., et al. 2006, Nature, 442, 786
Gerhard, O., Kronawitter, A., Saglia, R. B., & Bender, R. 2001, AJ, 121, 1936
Grazian, A., et al. 2007, A&A, 465, 393
Greve, T. R., et al. 2005, MNRAS, 359, 1165
Guilloteau, S., & Lucas, R. 2000, in Imaging at Radio through Submillimeter Wavelengths, ed. J. G. Mangum & S. J. E. Radford (San Francisco: ASP), 299
Guilloteau, S., et al. 1992, A&A, 262, 624
Hainline, L. J., Blain, A. W., Greve, T. R., Chapman, S. C., Smail, I., & Ivison, R. J. 2006, ApJ, 650, 614
Harayama, Y., Eisenhauer, F., & Martins, F. 2008, ApJ, 675, 1319
Hernquist, L. 1990, ApJ, 356, 359
Hinz, J. L., & Rieke, G. H. 2006, ApJ, 646, 872
Hopkins, P. F., Hernquist, L., Cox, T. J., di Matteo, T., Robertson, B., & Springel, V. 2006, ApJS, 163, 1
Hughes, D., et al. 1998, Nature, 394, 241
Israel, F. P. 2000, in Molecular Hydrogen in Space, ed. F. Combes & G. Pineau de Foréts (Cambridge: Cambridge Univ. Press), 326
———. 2005, A&A, 438, 855
Ivison, R. J, Smail, I., Frayer, D. T., Kneib, J.-P., & Blain, A. W. 2001, ApJ, 561, L45
Ivison, R. J., et al. 2002, MNRAS, 337, 1
Kassin, S. A., de Jong, R. S., & Weiner, B. 2006, ApJ, 643, 804
Kennicutt, R. C., Jr. 1998, ApJ, 498, 541
Khochfar, S., & Silk, J. 2006, ApJ, 648, L21
Kong, X., et al. 2006, ApJ, 638, 72
Kroupa, P. 2001, MNRAS, 322, 231
Lacey, C. G., Baugh, C. M., Frenk, C. S., Silva, L., Granato, G. L., & Bressan, A. 2008, MNRAS, 385, 1155
Law, D. R., Steidel, C. C., Erb, D. K., Larkin, J. E., Pettini, M., Shapley, A. E., & Wright, S. A. 2007, ApJ, 669, 929
Leroy, A., Bolatto, A., Walter, F., & Blitz, L. 2006, ApJ, 643, 825
Madden, S. C., Poglitsch, A., Geis, N., Stacey, G. J., & Townes, C. H. 1997, ApJ, 483, 200
Maloney, P., & Black, J. H. 1988, ApJ, 325, 389
Maloney, P. R., & Wolfire, M. G. 1997, in IAU Symp. 170, CO: Twenty-Five Years of Millimetre-Wave Spectroscopy, ed. W. B. Latter et al. (Dordrecht: Kluwer), 299
Maraston, C., et al. 2006, ApJ, 652, 85
Mihos, J. C., & Hernquist, L. 1994, ApJ, 431, L9
———. 1996, ApJ, 464, 641
Mo, H. J., & White, S. D. M. 2002, MNRAS, 336, 112
Naab, T., Johansson, P. H., Ostriker, J. P., & Efstathiou, G. 2007, ApJ, 658, 710
Naab, T., Khochfar, S., & Burkert, A. 2006, ApJ, 636, L81
Nagashima, M., Lacey, C. G., Okamoto, T., Baugh, C. M., Frenk, C. S., & Cole, S. 2005, MNRAS, 363, L31
Narayanan, D., et al. 2006, ApJ, 642, L107
———. 2008, ApJS, 176, 331
Nayakshin, S., & Sunyaev, R. 2005, MNRAS, 364, L23
Neri, R., et al. 2003, ApJ, 597, L113
Nesvadba, N. P. H., et al. 2007, ApJ, 657, 725
Nipoti, C., Londrillo, P., & Ciotti, L. 2003, MNRAS, 342, 501
Noeske, K. G., et al. 2007, ApJ, 660, L43
Oka, T., Hasegawa, T., Hayashi, M., Handa, T., & Sakamoto, S. 1998, ApJ, 493, 730
Papovich, C., et al. 2007, ApJ, 668, 45
Paumard, T., et al. 2006, ApJ, 643, 1011
Pettini, M., Shapley, A. E., Steidel, C. C., Cuby, J.-G., Dickinson, M., Moorwood, A. F. M., Adelberger, K. L., & Giavalisco, M. 2001, ApJ, 554, 981
Pettini, M., Steidel, C. C., Adelberger, K. L., Dickinson, M., & Giavalisco, M. 2000, ApJ, 528, 96
Pope, A., Borys, C., Scott, D., Conselice, C., Dickinson, M., & Mobasher, B. 2005, MNRAS, 358, 149
Reddy, N. A., Erb, D. K., Steidel, C. C., Shapley, A. E., Adelberger, K. L., & Pettini, M. 2005, ApJ, 633, 748
Renzini, A. 2005, in The Initial Mass Function Fifty Years Later, ed. E. Corbelli, F. Palle, & H. Zinnecker (Dordrecht: Kluwer), 221
Riechers, D. A., et al. 2006, ApJ, 650, 604
Rosolowsky, E., Engargiola, G., Plambeck, R. L., & Blitz, L. 2003, ApJ, 599, 258
Sakamoto, K., Scoville, N. Z., Yun, M. S., Crosas, M., Genzel, R., & Tacconi, L. J. 1999, ApJ, 514, 68
Sanders, D., & Mirabel, I. F. 1996, ARA&A, 34, 749
Satyapal, S., Watson, D. M., Pipher, J. L., Forrest, W. J., Greenhouse, M. A., Smith, H. A., Fischer, J., & Woodward, C. E. 1997, ApJ, 483, 148
Scoville, N. Z., Yun, M. S., & Bryant, P. M. 1997, ApJ, 484, 702
Scoville, N. Z., et al. 2000, AJ, 119, 991
Shapley, A. E., Erb, D. K., Pettini, M., Steidel, C. C., & Adelberger, K. L. 2004, ApJ, 612, 108
Shapley, A. E., Steidel, C. C, Adelberger, K. L, Dickinson, M., Giavalisco, M., & Pettini, M. 2001, ApJ, 562, 95
Shapley, A. E., Steidel, C. C., Erb, D. K., Reddy, N. A., Adelberger, K. L., Pettini, M., Barmby, P., & Huang, J. 2005, ApJ, 626, 698

Shen, S., Mo, H. J, White, S. D. M., Blanton, M. R., Kauffmann, G., Voges, W., Brinkmann, J., & Csabai, I. 2003, MNRAS, 343, 978
Shier, L. M., Rieke, M. J., & Rieke, G. H. 1994, ApJ, 433, L9
Smail, I., Chapman, S. C., Blain, A. W., & Ivison, R. J. 2004, ApJ, 616, 71
Smail, I., Chapman, S. C., Ivison, R. J., Blain, A. W., Takata, T., Heckman, T. M., Dunlop, J. S., & Sekiguchi, K. 2003, MNRAS, 342, 1185
Smail, I., Ivison, R. J., Blain, A. W., & Kneib, J.-P. 1998, ApJ, 507, L21
———. 2002, MNRAS, 331, 495
Smail, I., & Smith, G. P., & Ivison, R. J. 2005, ApJ, 631, 121
Smail, I., et al. 2007, ApJ, 654, L33
Solomon, P. M., & Barrett, J. W. 1991, in IAU Symp. 146, Dynamics of Galaxies and Their Molecular Cloud Distributions, ed. F. Combes & F. Casoli (Dordrecht: Kluwer), 235
Solomon, P. M., Downes, D., Radford, S. J. E., & Barrett, J. W. 1997, ApJ, 478, 144
Solomon, P. M., Rivolo, A. R., Barrett, J., & Yahil, A. 1987, ApJ, 319, 730
Spitzer, L., Jr. 1987, in Dynamics and Evolution of Globular Clusters (Princeton: Princeton Univ. Press)
Springel, V., et al. 2005, Nature, 435, 629
Steidel, C. C., Giavalisco, M., Pettini, M., Dickinson, M., & Adelberger, K. L. 1996, ApJ, 462, L17
Steidel, C. C., Shapley, A. E., Pettini, M., Adelberger, K. L., Erb, D. K., Reddy, N. A., & Hunt, M. P. 2004, ApJ, 604, 534
Stolte, A., Grebel, E. K., Brandner, W., & Figer, D. F. 2002, A&A, 394, 459
Strong, A. W., & Mattox, J. R. 1996, A&A, 308, L21
Swinbank, A. M., Chapman, S. C., Smail, I., Lindner, C., Borys, C., Blain, A. W., Ivison, R. J., & Lewis, G. F. 2006, MNRAS, 371, 465
Swinbank, A. M., Smail, I., Chapman, S. C., Blain, A. W., Ivison, R. J., & Keel, W. C. 2004, ApJ, 617, 64
Swinbank, A. M., et al. 2005, MNRAS, 359, 401
Tacconi, L. J., Genzel, R., Lutz, D., Rigopoulou, D., Baker, A. J., Iserlohe, C., & Tecza, M. 2002, ApJ, 580, 73
Tacconi, L. J., et al. 2006, ApJ, 640, 228
Tecza, M., et al. 2004, ApJ, 605, L109
Toft, S., et al. 2007, ApJ, 671, 285
Trujillo, I., Conselice, C., Bundy, K., Cooper, M. C., Eisenhardt, P., & Ellis, R. S. 2007, MNRAS, 382, 109
Trujillo, I., et al. 2006, MNRAS, 373, L36
van Dokkum, P. 2005, AJ, 130, 2647
———. 2008, ApJ, 674, 29
Weiss, A., Downes, D., Walter, F., & Henkel, C. 2005, A&A, 438, 533
———. 2007, in ASP Conf. Ser. 375, From *z*-Machines to ALMA: Submillimeter Spectroscopy of Galaxies, ed. A. J. Baker et al. (San Francisco: ASP), 25
Weiss, A., Neininger, N., Hüttemeister, S., & Klein, U. 2001, A&A, 365, 571
Wolfire, M., Hollenbach, D. J., & Tielens, A. G. G. M. 1993, ApJ, 402, 195
Wild, W., et al. 1992, A&A, 265, 447
Wilson, C. D. 1995, ApJ, 448, L97
Yee, H. K. C., Ellingson, E., Bechtold, J., Carlberg, R. G., & Cuillandre, J.-C. 1996, AJ, 111, 1783
Zirm, A. W., et al. 2007, ApJ, 656, 66